China Geology 8 (2025) 707−724

China Geology

Journal homepage: http://chinageology.cgs.cn
https://www.sciencedirect.com/journal/china-geology

Shale gas prospect of the Lower Permian in the South Yellow Sea Basin of the Lower Yangtze area: Insights from the whole-cored CSDP-2 borehole

Yu-mao Pang[a, b,*], Zhao-meng Wei[a], Xing-wei Guo[c, d], Chuan-sheng Yang[b, c,*], Rui-shan Ma[e], Xun-hua Zhang[b, c, d]

[a] *College of Earth Science and Engineering, Shandong University of Science and Technology, Qingdao* 266590, *China*
[b] *Qingdao Marine Science and Technology Center, Laoshan laboratory, Qingdao* 266237, *China*
[c] *Qingdao Institute of Marine Geology, China Geological Survey, Ministry of Natural Resources, Qingdao* 266071, *China*
[d] *Institute of Marine Science and Technology, Shandong University, Qingdao* 266237, *China*
[e] *PetroChina Qinghai Oilfield Company, Dunhuang* 736202, *China*

ARTICLE INFO

Article history:
Received 23 December 2023
Received in revised form 2 March 2024
Accepted 11 March 2024
Available online 14 March 2025

Keywords:
Shale gas
Continental Shelf Drilling Program
South Yellow Sea Basin
Lower Yangtze Platform
Lower Permian
Shale reservoir evaluation
Oil-gas exploration engineering

ABSTRACT

Shale gas is abundant in the Paleozoic of the Yangtze Platform, and several high-yield shale gas fields have been built in the Upper Yangtze Platform, China. The Permian of the South Yellow Sea Basin (SYSB) in the Lower Yangtze area is considered a potential target for shale gas exploration; however, the fundamental geological conditions of shale gas have not been studied. Based on the first whole-cored scientific drilling borehole (CSDP-2) in the SYSB, detailed tests involving petrology, organic geochemistry, and reservoir physical properties were conducted to evaluate the shale gas potential of the Lower Permian. The Lower Permian is dominated by organic-rich siliceous, clay, and clay-mixed shales. The average total organic carbon content is 5.99%, and the organic matter is mainly type II_1–II_2, which has entered the high-over mature evolution stage. The pore types of organic-rich shales mainly include organic pores, dissolution pores, and intergranular pores, of which the meso-/macropores are well developed. The average porosity is 3.04%, and the total specific surface area and pore volume are 3.47 m^2/g and 7.21×10^{-3} cm^3/g, respectively. The average Langmuir volume obtained from the methane adsorption isotherms is 2.70 cm^3/g, and methane is mainly adsorbed in the meso-/macropores. The lower Permian shales are rich in methane as indicated by gas logging results, with an average content of 7.3%, which can reach up to 65.9%. A comparison of the study area with typical shale gas fields shows that the Lower Permian is brittle and shallowly buried and has a high potential for shale gas exploration and low-cost development. The depression areas of the SYSB are overlain by thick Mesozoic–Cenozoic sediments, show higher organic matter maturity, and may have greater shale gas potential. The shale gas exploration breakthrough of the study area is of great significance to ensure the energy supply of economically developed areas on the east China.

1. Introduction

Clean shale gas resources have gradually become an important growth point for China's natural gas industry and are beneficial for achieving the "carbon peak and carbon neutrality" goal. Paleozoic marine and transitional shales in the Yangtze Platform have great prospects for natural gas exploration, and significant exploration breakthroughs have been made in the Cambrian, Ordovician–Silurian, and Permian (He ZL et al., 2016; Zou CN et al., 2016; Jiang ZX et al., 2020). At present, China is the largest shale gas production area after North America, and the main exploration and development area is distributed on the Yangtze Platform, in South China (Zou CN et al., 2021; Nie HK et al., 2022). The Yangtze Platform can be divided into the upper, middle, and lower regions according to their tectonic positions, and the degree of shale gas exploration varies significantly (Zhao WZ et al., 2016; Zou CN et al., 2021). The Upper Yangtze Platform (UYP) is currently the

First author: *E-mail address*: pangyumao14@mails.ucas.ac.cn (Yu-mao Pang).

* Corresponding author: *E-mail address*: pangyumao14@mails.ucas.ac.cn (Yu-mao Pang); ychuansheng@mail.cgs.gov.cn (Chuan-sheng Yang).

Literary editor: Li-qiong Jia
doi:10.31035/cg2023153
2096-5192/© 2025 China Geology Editorial Office.

main shale gas-producing area in China (Fig. 1). However, the exploration degree of the Lower Yangtze Platform (LYP) is extremely low; therefore, evaluation of shale gas potential needs to be carried out urgently.

In recent years, high-yielding shale gas reservoirs have been discovered from the Upper Ordovician Wufeng Formation to the Lower Silurian Longmaxi Formation (O_3w-S_1l) of the Weiyuan, Changning, Zhaotong, Fushun-Yongchuan, and Fuling areas in Sichuan Basin, UYP, China (Zhao WZ et al., 2016; Hu H et al., 2021). In 2019, the daily gas production of Lu203 well in the Sichuan Basin reached 137.9×10^4 m^3/d, becoming the first shale gas well in China with a daily production of more than one million cubic meters. In 2020, the gas production of the strata above 3500 m in the Sichuan Basin exceeded 200×10^8 m^3, and the recoverable reserves exceeded 5900×10^8 m^3, indicating a huge potential for shale gas exploration in the UYP (Zou CN et al., 2021). Well Leiye 1 (2023), a shale gas exploration well in the Sichuan Basin, has made a breakthrough in shale gas exploration in the Permian. In addition, the Eyi-1, Eyi-2, and Eyang-1 wells in the Middle Yangtze Platform show good prospects for shale gas resources (Jiang ZX et al., 2020). Multiple shale gas exploration wells in northern Jiangsu, southern Anhui, and northern Zhejiang in the LYP also reveal good prospects for shale gas in the Permian system (Zheng HJ et al., 2020). Well JY1 in southern Anhui of Lower Yangtze drilled by the China Geological Survey shows a good shale gas prospect in the Upper Permian (Li QQ et al., 2022). However, shale gas exploration in the LYP is still in an initial stage. The study on the Paleozoic shale gas potential of the South Yellow Sea basin (SYSB), which is the main tectonic body of the LYP, is still lacking. In 2016, with the support of the Continental Shelf Drilling Program (CSDP), a whole-cored scientific borehole (CSDP-2) was drilled in the Central Uplift of the SYSB (Fig. 1). The CSDP-2 borehole encountered thick Paleozoic marine deposits, of which the thickness of Permian was 857.7 m with thick dark mudstone and significant gas logging anomalies (Fig. 1). The Permian shale gas exploration of the SYSB in the LYP is important for securing China's energy supply.

In this study, petrology, mineralogy, organic geochemistry, rock physical properties, and maceral analyses were carried out on the Lower Permian shales drilled from the CSDP-2 wells. Detailed test data of organic matter abundance, type, and thermal maturity were used to evaluate the hydrocarbon generation potential of the Lower Permian shales in the study area. X-ray diffraction (XRD), scanning electron microscopy (SEM), low-pressure N_2 adsorption–

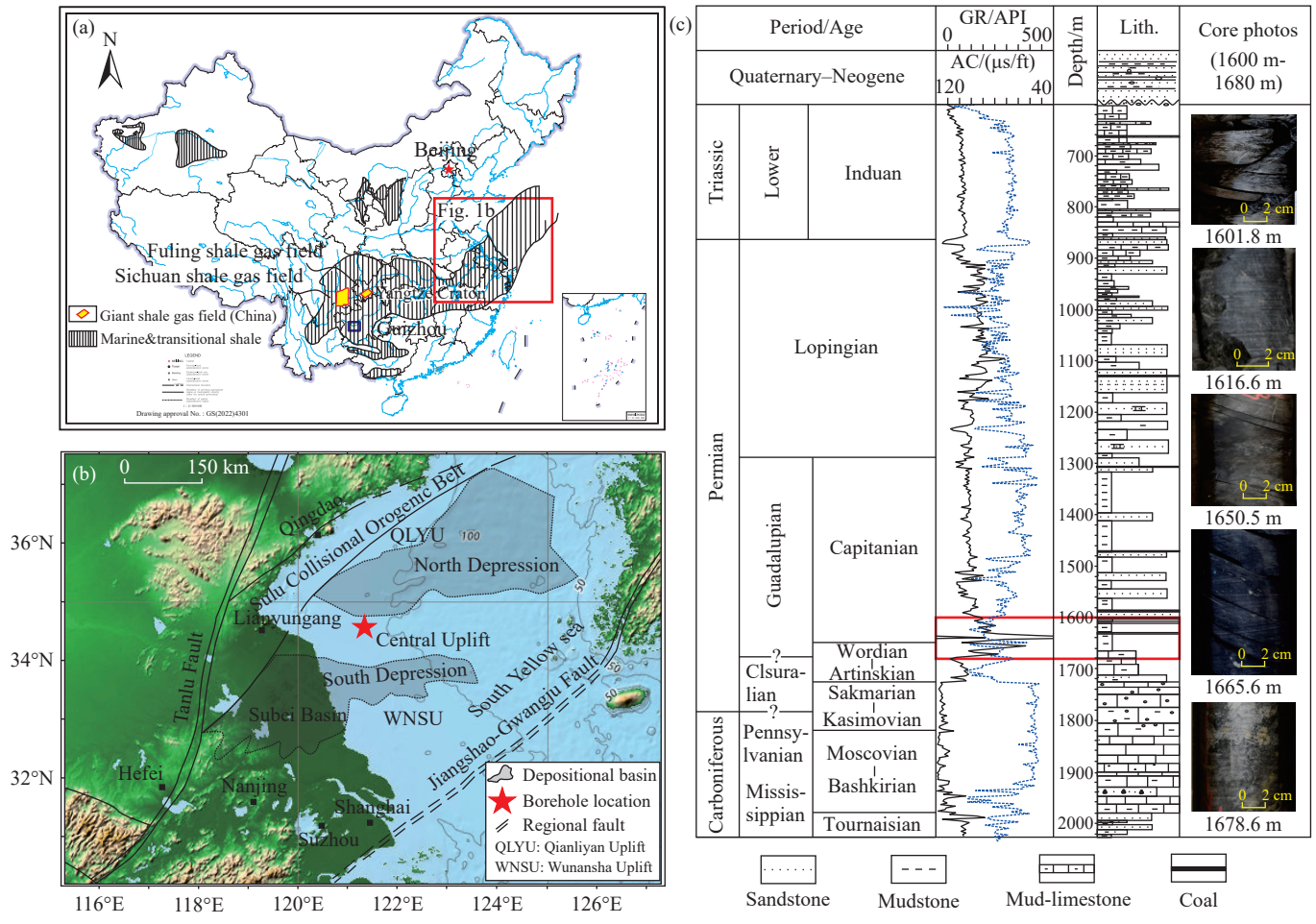

Fig. 1. a–Geographical map of the South Yellow Sea Basin, the distribution areas of marine and transitional shale, China (modified from Zou CN et al., 2021); b–geological map of the Lower Yangtze Platform and the CSDP-2 borehole location; and c–chronostratigraphic chart of the CSDP-2 borehole from 600 m to 2000 m with the red solid line box marks the interval of gas logging anomaly.

desorption, high-pressure methane isothermal adsorption, and nuclear magnetic resonance (NMR) analyses of the shale samples were performed to evaluate the mineral composition, pore structure, and reservoir properties. Finally, the main geological parameters of typical shale gas fields in China and abroad were compared to evaluate the exploration prospects of Permian shale gas in the study area.

2. Geologic setting and the CSDP-2 borehole

The Yellow Sea is situated between the Chinese mainland and the Korean Peninsula and is geographically separated into the North Yellow Sea and the South Yellow Sea by the Qinling-Dabie-Sulu collision orogenic belt, which was formed as a result of the Indo-Chinese tectonic movement (Gilder S and Courtillot V, 1997; Liu J et al., 2018). The SYSB belongs to the LYP and is a large-scale superimposed sedimentary basin with Paleozoic marine and Meso–Cenozoic continental rifted deposits (Pang YM et al., 2021). The stratigraphic units of the SYSB consist of Precambrian metamorphic basement rocks, Paleozoic to Triassic marine craton sediments, and overlying continental rifted deposits (Liu J et al., 2018).

The SYSB can be subdivided into several sub-tectonic units, of which the main units from north to south are the Qianliyan Uplift, North Depression, Central Uplift, South Depression, and Wunansha Uplift (Pang YM et al., 2018). The marine strata are widespread in the entire basin, whereas the Meso–Cenozoic continental sediments are developed mainly within the North Depression and South Depression. The Meso–Cenozoic sediments of the depressions are more than 8 km thick but are usually absent in the Central Uplift. Recently, geological surveys have revealed the development of thick Paleozoic marine strata under the Neogene in the Central Uplift, which have become important potential targets for hydrocarbon exploration.

With the support of the China Geological Survey, the whole-cored CSDP-2 borehole was drilled in the Central Uplift of the SYSB to reveal the Paleozoic lithological attributes and its petroleum prospects. The CSDP-2 borehole is the first deep-drilling borehole in the Central Uplift and was drilled to a depth of 2843.4 m. A 2700 m core was recovered, confirming the presence of thick Paleozoic marine deposits in the Central Uplift. The CSDP-2 also revealed multiple oil displays from the Permian cores and significant gas logging anomalies in some intervals for the first time, showing a good oil and gas exploration potential.

3. Samples and methods

To evaluate the shale gas potential of the Lower Permian in the study area, total organic carbon content (TOC), vitrinite reflectance (Ro), Rock-Eval pyrolysis, XRD, SEM, organic maceral component, NMR, low-pressure nitrogen adsorption–desorption, and high-pressure methane isothermal adsorption analyses were carried out on shale samples of CSDP-2.

3.1. Total organic carbon and mineral composition

A CS-230 Carbon and Sulfur Analyzer (American LECO company) was used to test the TOC. The sample was burned in a high-temperature oxygen environment after removing inorganic carbon with dilute hydrochloric acid, and the produced carbon dioxide was detected using an infrared detector to obtain TOC.

An X-ray diffractometer (ULTIMA-IV, Japanese RIGAKU company) was used to test the mineralogical composition according to the industry specifications (Analysis method for clay minerals and ordinary non-clay minerals in sedimentary rocks by the X-ray diffraction, SY/T 5163-2018, China), with a scanning speed of 2°/min.

3.2. Rock-Eval pyrolysis

A Rock-Eval instrument (Classic S3, France VINCI company) was used for rock pyrolysis. The temperature was first set at 300°C for 3 min to capture the free hydrocarbons (S_1), then increased to 600°C for 1 min to obtain the pyrolytic hydrocarbons (S_2), and the carbon dioxide (S_3) and maximum pyrolysis temperature (T_{max}) would be obtained during the next 4 min. The oxygen index (OI), hydrogen index (HI), and production index (PI) were calculated as follows: OI = S_3 × 100/TOC (mg CO2/g TOC), HI = S_2 × 100/TOC (mg HC/g TOC), and PI = S_1 / (S_1 + S_2).

3.3. Organic petrology and scanning electron microscope

Maceral fluorescence analysis was performed to evaluate the maceral composition and thermal maturity. The samples were impregnated with epoxy resin, ground with silicon carbide and diamond gravel, and polished with isopropyl alcohol, alumina slurry, and silk. The processed samples were examined using a microscope to measure the percentage of reflected incident light and maceral composition. A field emission-scanning electron microscope (QUANTA 200F, American FEI company) was used for maceral analysis. The sample slices were hand-polished on stubs and then polished using argon-ion milling to obtain a flat surface. The back-scattered electron and secondary electron images magnified 500–15000 times were collected on a flat surface.

3.4. Nuclear magnetic resonance

The NMR spectrometer (MesoMR23-060H–I, China) with a 21.36 MHz resonance frequency for ^1H at a low magnetic field of 0.52 T was used to obtain T2 spectra using the Carr-Purcell-Meiboom-Gill (CPMG) sequence, with measurement parameters of TE (echo time): 0.07 ms, TW (waiting time): 3000 ms, NS (number of scans): 64, and NECH (echo number): 6000.

The sample was dried in a vacuum oven at 110°C for 24 h after washed with oil, and the original NMR relaxation spectra was obtained by NMR test. Subsequently, the dried sample was evacuated for 24 h and then saturated with C_{12} at

10 MPa for 24 h. The saturated NMR relaxation spectra of C_{12}-saturated samples was obtained. The masses of the dried and C_{12}-saturated samples were recorded simultaneously to calculate the weighted porosity, which was used as a reference for the NMR porosity.

3.5. Low-pressure N_2 adsorption–desorption

Low-pressure N_2 adsorption–desorption test was conducted using a Micromeritics specific surface area and porosity analyzer (ASAP 2460, American MICROMERITICS company). The shale sample was crushed into 40–60 mesh and dried at 383 K for 24 h in a vacuum oven. N_2 adsorption–desorption isotherms were collected at 77 K with P/P_0 ranging from 0.01 to 0.993. The specific surface area (SSA), pore volume (PV), and pore size distribution (PSD) were calculated using the adsorption branch. PV was the single pore volume at a P/P_0 of approximately 0.99, while SSA was determined using the BET method according to the adsorption data with P/P_0 between 0.05 and 0.35 (Brunauer S et al., 1938). The PSD was calculated using the Barrett-Joyner-Halenda (BJH) model (Brunauer S et al., 1938).

3.6. High-pressure methane isothermal adsorption

High-pressure methane isothermal adsorption tests were performed using a high-pressure gas-adsorption instrument (3H-2000PH690, Instrument Technology Co., LTD, Beijing). The sample was crushed into 40–60 mesh and then dried at 383 K for 24 h. A detailed test process and data calculation were conducted according to the National standard (Determination methods of methane isothermal adsorption in shale Part 1: Capacity method, GB/T 35210.1-2017, China). The reference and sample cells were set at a consistent temperature of 40°C (±0.1°C). Methane sorption capacities were measured up to a pressure of approximately 22 MPa.

The Langmuir-based excess adsorption model was used to fit the sorption pressure (P) and excess sorption capacity (V_{ex}) and calculate the absolute sorption capacity (V_{ab}) as follows (Equs. 1, 2):

$$V_{ex} = \frac{V_L P}{P_L + P}\left(1 - \frac{\rho_g}{\rho_a}\right) \tag{1}$$

$$V_{ab} = \frac{V_L P}{P_L + P} \tag{2}$$

where V_L and P_L are the Langmuir volume (cm^3/g) and pressure (MPa), respectively; P_L is the pressure where the methane adsorbed amount equals half of the maximum methane sorption capacity (V_L); ρ_a and ρ_g are the densities (g/cm^3) of the adsorbed and free methane, respectively.

3.7. Fractal dimension calculation

Fractal dimension can be used to describe the pore structure and surface irregularities of porous media (Cai YD et al., 2013; Wang JY and Guo SB, 2021). Various fractal dimension calculation models, including the BET model, the Frenkel-Halsey-Hill (FHH) model, and thermodynamic methods, have been proposed and widely applied (Levitz P et al., 1988; Pfeifer P et al., 1989; Tatlıer M and Erdem-Şenatalar A, 1999; Cao TT et al., 2016; Zhang JZ et al., 2018). In this study, the fractal dimension was calculated using the FHH model (Equ. 3).

$$ln\left(\frac{V}{V_0}\right) = C + (D-3)\cdot ln\left(ln\left(\frac{P_0}{P}\right)\right) \tag{3}$$

where D is the fractal dimension; C is a constant; V is the gas adsorption volume (cm^3/g) under equilibrium pressure (P, MPa); V_0 is the volume of the monomolecular layer (cm^3); P_0 is the saturated vapor pressure (MPa).

4. Results

4.1. Petrological characteristics of the Lower Permian shales in SYSB

4.1.1. Mineral composition

The mineral compositions of the shale samples collected from the CSDP-2 borehole are listed in Table 1. The results show that the shale minerals mainly include quartz, clay minerals, and calcite, followed by pyrite and feldspar. The clay mineral contents range from 1.8% to 57.0%, with an average of 33.1%, among which the average contents of illite and mixed illite/smectite are 39.6% and 26.6%, respectively. The average contents of siliceous minerals (quartz and feldspar) and calcareous minerals (calcite and dolomite) are 39.6% and 19.4%, respectively. The presence of brittle minerals is beneficial for the formation of natural and artificially induced fractures.

According to the compositions of the shale minerals, the 1600–1680 m interval of the Lower Permian can be divided into upper (Layer_1) and lower (Layer_2) layers (Table 1). Layer_1 is mainly siliceous minerals with an average content of 48.0%, and the calcium mineral content is 7.6%. Layer_2 is mainly composed of calcium minerals with an average content of 35.4%, while the average content of siliceous minerals is 28.4%. The clay minerals in Layer_1 and Layer_2 are similar, but the mixed illite/smectite content is higher in Layer_2. Almost all shale samples contain pyrite with an average content of 6.7%, which is more abundant in Layer_1.

4.1.2. Shale lithofacies

Considering the contents of siliceous minerals, calcareous minerals, and clay minerals as the three terminal elements, shale lithofacies are divided into siliceous shale (SiS), calcareous shale (CaS), clay shale (ClS), siliceous mixed shale (SiMS), calcareous mixed shale (CaMS) and clay mixed shale (ClMS) (Table 1; Fig. 2). According to the TOC content of the shale, it is divided into organic-poor (<1%), organic-medium (1%–3%), and organic-rich shale (>3%).

Layer_1 was dominated by organic-rich SiS, followed by medium-rich organic ClS and ClMS, with a TOC of

Table 1. Total organic carbon (TOC), rock-mineral composition and lithofacies classification of the Lower Permian shale samples in the South Yellow Sea Basin.

Layer	Depth/m	Mineral composition /%											Clay mineral composition /%				Lithofacies	
		TOC	Siliceous minerals			Calcareous minerals			Siderite	Pyrite	Anatase	Iro-dolomite	Clay					Type	Organic abundance
			Quartz	Feldspar	Total	Calcite	Dolomite	Total						Illite	Illite/smectite	Chlorite	Kaolinite		
Layer_1	1601.8	1.63	31.4	2.4	33.8	0	7.1	7.1	3	5.9	1.3	0	48.9	0	0	/	/	ClMS	Medium
	1609.7	1.53	28.7	3.7	32.4	0	6.7	6.7	0	7.3	1	0	52.6	0	0	/	/	ClS	Medium
	1611.88	/	51	5.5	56.8	0	1.6	1.6	0.7	4.9	/	/	36.4	87.8	/	0	12.2	SiS	/
	1615.3	6.15	25.1	3.3	28.4	0	8.9	8.9	0	10.4	1	0	51.3	0	0	/	/	ClS	Rich
	1617.78	/	44.5	14.6	59.1	3.7	6.9	10.6	0	8.2	/	/	22.1	90.4	/	2	7.6	SiS	/
	1619.6	7.58	27.8	3.6	31.4	0	12.8	12.8	0	13.2	1.8	0	40.8	0	0	/	/	ClMS	Rich
	1625	6.03	25.7	3.8	29.5	0	11.6	11.6	0	12.5	1.1	0	45.3	0	0	/	/	ClMS	Rich
	1626.5	5.66	24.1	3.1	27.2	0	0	0	0	14.7	1.1	0	57	0	0	/	/	ClS	Rich
	1627.5	2.43	21.7	5.2	26.9	0	9	9	0	9.3	1.1	0	53.7	0	0	/	/	ClS	Medium
	1629	/	53.6	6.4	60	0	0.5	0.5	0	14.2	/	/	25.3	100	/	0	0	SiS	/
	1630.2	5.1	23.8	3.7	27.5	0	11.4	11.4	0	12.1	0.8	0	48.2	0	0	/	/	ClMS	Rich
	1632.9	16.21	47.7	7.3	55	0	7.7	7.7	0	9	1.5	0	26.8	0	0	/	/	SiS	Rich
	1634.1	6.17	24.8	9.8	34.6	0	8.4	8.4	0	3	0	0	54	0	0	/	/	ClS	Rich
	1634.48	/	53.2	13.3	66.4	0	1.4	1.4	0.3	13.4	/	/	18.4	100	/	0	0	SiS	/
	1640.2	7.96	89.2	0.8	90	0.6	0	0.6	0.3	1.7	0	0	7.4	0	0	/	/	SiS	Rich
	1642.78	/	83.6	4.6	88.2	0	1.6	1.6	0	3.3	/	/	6.8	100	/	0	0	SiS	/
	1645.3	6.41	47.6	3.2	50.8	5	0	5	4.1	10.1	0	0	30	0	0	/	/	SiS	Rich
	1649	6.91	37	7.7	44.7	4.7	26.9	31.6	4.5	7.2	0	0	12	0	0	/	/	SiMS	Rich
	1651.9	5.6	66	2.7	68.7	2.2	5.8	8	0	3.9	0	0	19.4	77	23	0	/	SiS	Rich
Layer_2	1653.2	11.29	48.7	2.5	51.2	10	5.2	15.2	0	6.6	0	0	27	72	28	0	/	SiS	Rich
	1655.58	/	27.6	8.6	36.2	9.4	51.4	60.8	0	1.2	/	/	1.8	84.1	/	15.9	0	CaS	/
	1657.2	6.9	23	4.3	27.3	12.7	11.9	24.6	0	5.4	1.4	0	41.3	62	38	0	/	ClMS	Rich
	1661.5	3.63	18.7	2.1	20.8	25.5	14.7	40.2	0	2.9	0	0	36.1	22	78	0	/	CaMS	Rich
	1662.1	3.42	17.3	1.5	18.8	19.3	6.9	26.2	0	2.2	1.4	0	51.4	12	88	0	/	ClS	Rich
	1665.6	1.44	24.5	3.7	28.2	21.1	8.5	29.6	0	4.6	0.6	0	37	26	74	0	/	ClMS	Medium
	1665.78	/	23.5	11.7	35.2	48.3	0.8	49.1	2.8	7	/	/	6	94.6	/	5.4	0	CaMS	/
	1666.3	6.84	13.4	3.2	16.6	19.1	0	19.1	0	1.8	1.2	8.4	52.9	23	77	0	/	ClS	Rich
	1670.7	4.33	18	2.8	20.8	21.1	10	31.1	0.4	3	0	0	44.7	16	84	0	/	ClMS	Rich
	1671.5	13.13	21.7	3.2	24.9	12.7	13.8	26.5	3.5	8	0	0	37.1	58	42	0	/	ClMS	Rich
	1673.88	/	20.7	3.2	23.9	50.5	6.9	57.4	2.7	3.6	/	/	12.4	93.6	/	2.4	4	CaS	/
	1675.48	/	2.7	1.4	4.1	59	34	93	0	0.9	/	/	2	88.6	/	6.4	5	CaS	/
	1678.6	1.43	42.2	0	42.2	0	0	0	1	9.1	0	12.6	35.1	14	80	6	/	SiMS	Medium
	1679.18	/	17.2	29.9	47.1	1.2	0.9	2.1	0	1	/	/	49.9	84.7	/	4.7	10.6	ClMS	/

Notes: SiS: siliceous shale; CaS: calcareous shale; ClS: clay shale; SiMS: siliceous mixed shale; CaMS: calcareous mixed shale; ClMS: clay mixed shale.

1.53%–16.21% (average 6.1%). Layer_2 was dominated by medium-rich organic ClMS, with a small amount of organic-rich CaS and CaMS. The siliceous mineral content is similar to that of Layer_1, but the calcareous mineral content is higher. The development of dissolution pores and fractures in calcareous minerals is conducive to improving the shale reservoir capacity. Compared with the shales in Layer_1, the clay minerals in the shales of Layer_2 have a higher content of illite and mixed illite/smectite, providing some additional micropores. The TOC in Layer_2 is 1.43%–13.13%, with an average value of 5.82%, which is similar to that of Layer_1.

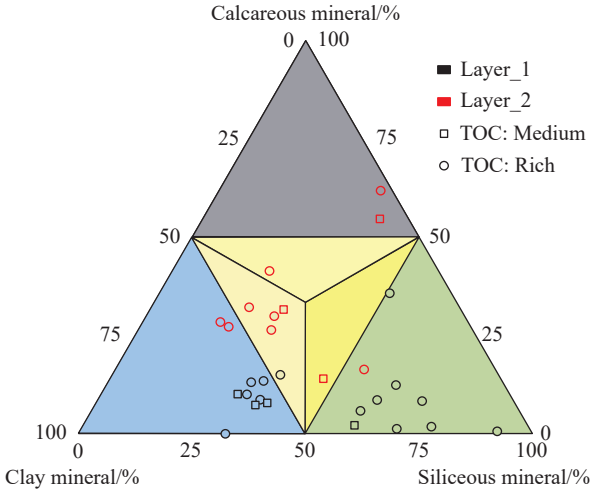

Fig. 2. Triangular plot analysis of clay, calcareous minerals, and siliceous minerals of the Lower Permian shale and organic matter enrichment. TOC: Total organic carbon content.

4.1.3. Organic petrological characteristics

(i) Abundance of organic matter

The TOC of the Lower Permian shale ranges from 1.43% to 16.21%, with an average value of 5.99%. Among them, the TOC in the interval of 1640–1658 m is 5.60%–11.29%, with an average value of 7.51%. The hydrocarbon potential (Pg) ranges from 0.15 mg HC/g rock to 3.64 mg HC/g rock, with an average value of 0.95 mg HC/g rock. Generally, SiS and SiMS in Layer_1 and CaMS, SiS, and ClS in Layer_2 have good hydrocarbon generation potential.

(ii) Kerogen type

The pyrolysis hydrogen index (HI) and highest pyrolysis peak temperature (T_{max}) of the rock reflect the type of shale organic matter. Plotting analysis of the pyrolysis parameters also shows that the organic matter of the Lower Permian shales is dominated by type II_2–III (Figs. 3a, b).

Detailed identification of the organic maceral components was carried out on six samples to further clarify the organic matter types. Maceral analysis revealed that the Lower

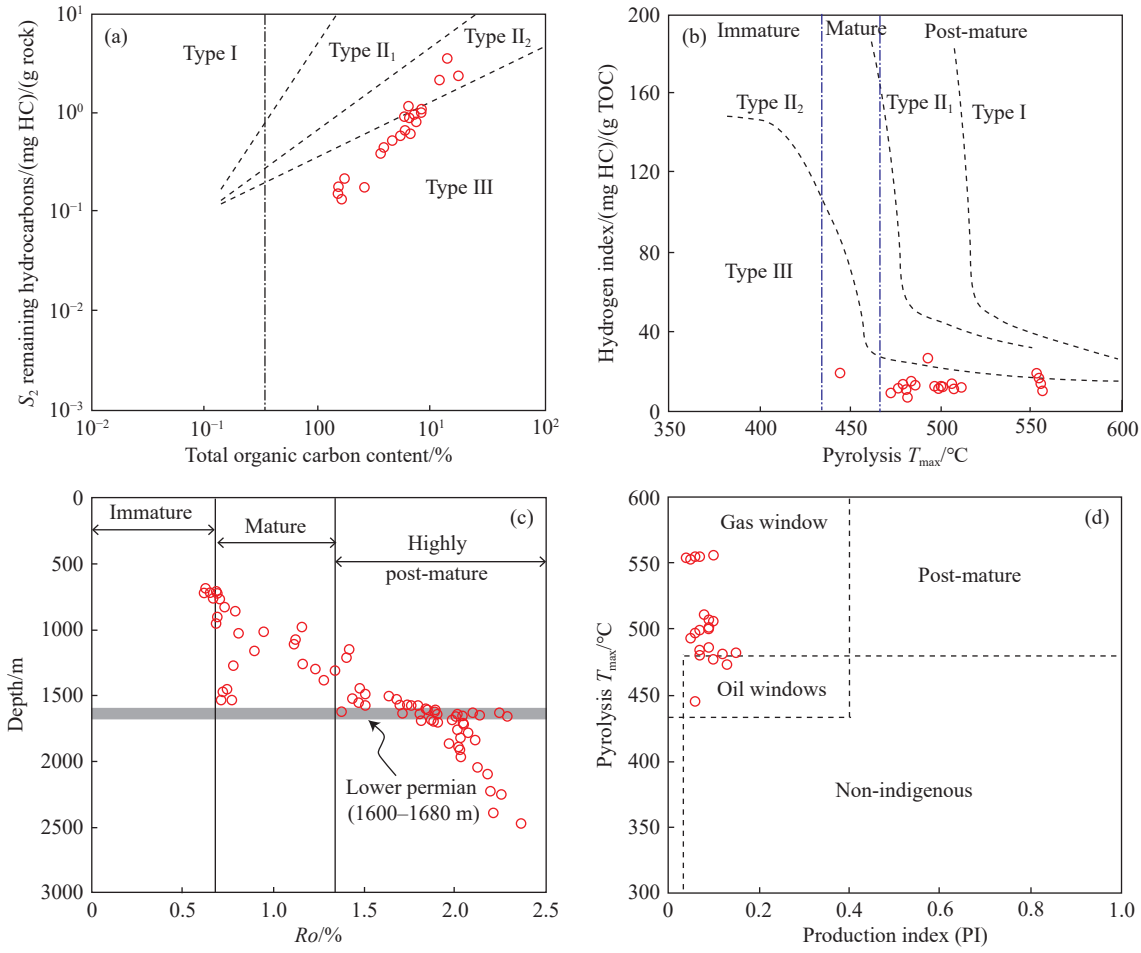

Fig. 3. Types of organic matter of the Lower Permian shales constrained by rock pyrolysis data (a, b); Relationship between vitrinite reflectance and depth of CSDP-2 core samples (c) and plot analysis of pyrolysis T_{max} and production index (d).

Permian shales are dominated by kerogen types II_1–II_2 (Table 2). The samples are rich in exinite (average 74.5%), and the main component is an amorphous mass. The average content of vitrinite is 18.6%. The content of inertinite is low, and some samples contain saprophytic mass.

(iii) Thermal maturity

The vitrinite reflectance (*R*o) analysis of the CSDP-2 core samples shows that the Paleozoic shales have entered the high-over mature stage (Fig. 3c). The measured *R*o values of the shale samples at 1562.00 m, 1578.30 m, 1586.50 m, and 1599.20 m are 1.47%, 1.23%, 1.50%, and 1.52%, respectively, indicating that the Lower Permian shale is in the mature–high-over mature stage. Plotting analysis of the pyrolysis parameters also shows that the Lower Permian shale has entered the gas window (Fig. 3d).

4.2. Reservoir evaluation of the Lower Permian shales

4.2.1. Pore types

The SEM images show that the shale pores mainly include organic pores, dissolution pores, intergranular pores, microfractures, and pores within clay mineral grains (Fig. 4), which provide abundant reservoir space for shale gas. The organic pores are mainly pitted, honeycombed, and subspherical in shape (Figs. 4d, g, h). The high content of calcareous minerals in the CaS and CaMS shales not only facilitates the generation of microfractures but also leads to more prevalent dissolution pores (Figs. 4c, e, h). Microfractures can significantly improve the shale permeability and reservoir capacity. The SEM images show that the microfractures are usually developed near the contact zone between organic and inorganic minerals and inside brittle mineral grains. Organic pores, dissolution pores, and intergranular pores are the most developed in organic-rich shales, followed by microfractures and intra-grain pores of clay minerals. In general, organic pores are more developed in highly mature organic-rich ClMS and ClS shales, whereas intergranular pores, dissolution pores, and microfractures are more abundant in SiS, CaS, and CaMS shales.

4.2.2. Nuclear magnetic resonance porosity of shale samples

With the advantages of rapid, nondestructive, and in-situ detection, NMR analysis can effectively compensate for the shortcomings of conventional reservoir analysis methods and has been widely used for shale reservoir evaluation. In this study, the weighted porosity of the measured shale samples and NMR porosity are highly correlated ($R2 = 0.959$), indicating the high reliability of the NMR porosity results (Fig. 5). The NMR porosity (NMR porosity) of the 26 shale samples range from 1.42% to 6.13%, with an average of 3.04% (Table 3).

4.2.3. Nitrogen adsorption–desorption results

Nitrogen adsorption experiments are an effective method for obtaining pore structure parameters, such as pore volume (PV), specific surface area (SSA), and pore size distribution of shale. The results show that the total specific surface area (TSSA) of the Lower Permian shales ranges from 0.30 m^2/g to 11.50 m^2/g, with an average value of 3.47 m^2/g. The total pore volume (TPV) ranges from 1.38×10^{-3} cm^3/g to 13.71×10^{-3} cm^3/g, with an average of 7.21×10^{-3} cm^3/g. The average pore diameter (d_{Na}) ranges from 4.49 nm to 33.63 nm, with an average value of 13.64 nm (Table 3). The average TSSA and TPV of shales in Layer_1 are 1.88 m^2/g and 5.57×10^{-3} cm^3/g, respectively, whereas the corresponding values in Layer_2 are 5.76 m^2/g and 9.58×10^{-3} cm^3/g, respectively, showing that Layer_2 has higher shale gas storage capacity. However, the d_{Na} of the sample in Layer_1 is 17.77 nm, which is higher than the 7.66 nm of d_{Na} in Layer_2.

According to the pore type classification results of the International Union of Pure and Applied Chemistry (IUPAC), shale pores are classified into micropores (<2 nm), mesopores (2–50 nm), and macropores (>50 nm) based on pore size. The shales in the study area are predominantly mesoporous, and the development of micropores and macropores in Layer_1 and Layer_2 differs greatly (Fig. 6). The contributions of micro-, meso-, and macropores to the SSA of shales in Layer_1 are 5.58%, 85.33%, and 9.09%, respectively. The contributions of micro-, meso-, and macropores to the SSA of the shales in Layer_2 are 12.73%, 84.44%, and 2.83%, respectively. Overall, mesopores contribute the most to the SSA of the shale (Figs. 6a, c). The SSA of the micropores of the shale samples in Layer_2 is 2–3 times larger than that of Layer_1. This is possibly due to the high content of calcareous minerals in Layer_2, which develops more dissolution pores (Fig. 4). The high content of illite in the clay minerals may also lead to more micropores (Fig. 4). In addition, the organic matter of highly mature shales produces

Table 2. Maceral composition for shale samples and kerogen types.

Depth/m	Sapropelinite/%	Exinite/%						Vitrinite/%			Inertinite/%	TI	Type
	Saprophytic mass	Resinite	Cutinite	Sporinite	Mycetome	Amorphous mass	Total	Hydrogen-rich vitrinite	Normal vitrinite	Total	Fusinite		
1599.2	/	/	0.41	0.82	/	74.59	75.82	2.87	18.44	21.31	2.87	21.5	II_2
1619.28	11.33	/	/	/	0.39	77.73	78.13	1.56	7.81	9.38	1.17	43.52	II_1
1634.3	/	/	/	0.49	/	91.22	91.71	0.98	6.83	7.8	0.49	40.34	II_1
1650.1	/	/	/	/	/	88.41	88.41	1.93	9.18	11.11	0.48	37.03	II_2
1660.6	4.8	/	/	0.44	/	79.91	80.35	1.75	12.66	14.41	0.44	35.22	II_2
1706.78	19	/	/	1.5	/	31	32.5	3	44.5	47.5	1	1.18	II_2

Notes: TI=(100A+50B-75C-100D)/100, where A, B, C and D refer to the percentage of sapropelinite, exinite, vitrinite and inertinite marcel, respectively.

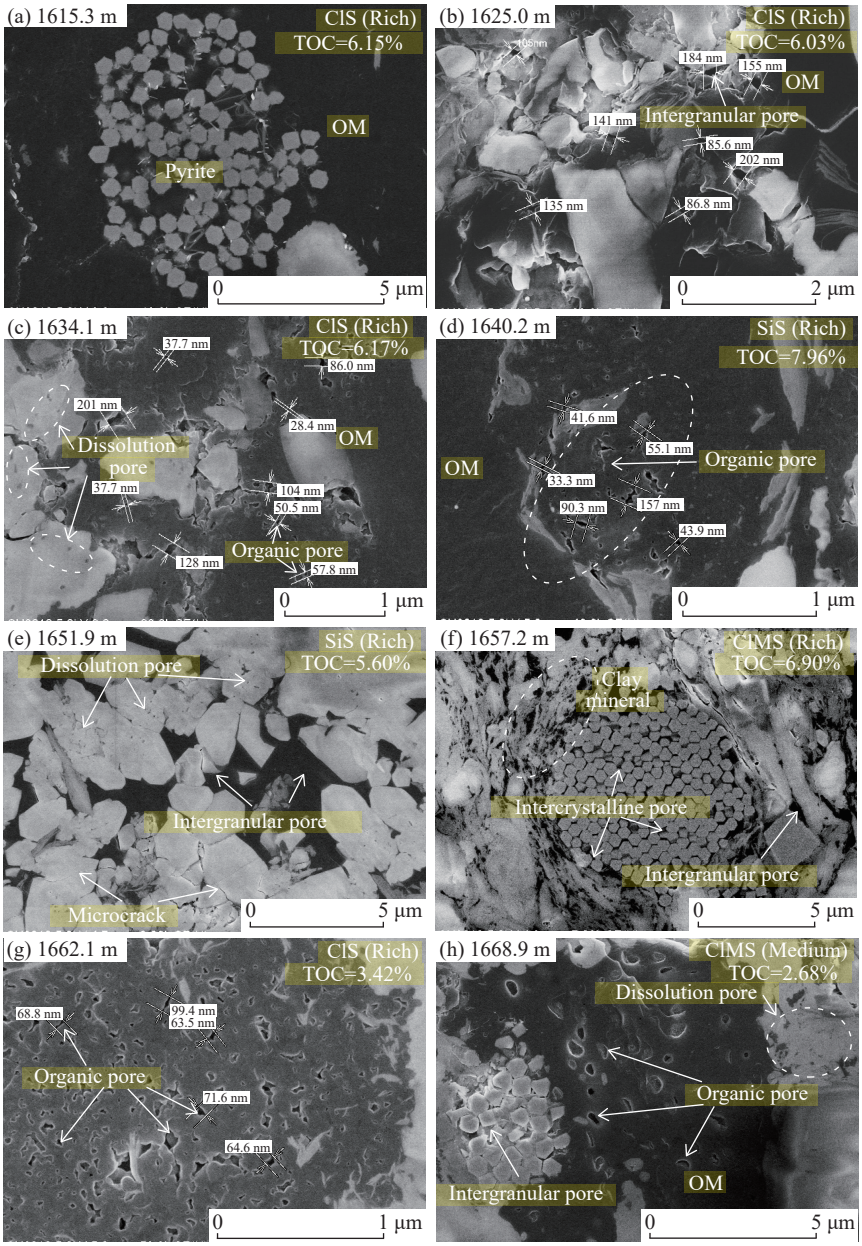

Fig. 4. Scanning electron microscopy (SEM) images show pore development characteristics of the Lower Permian shale in the South Yellow Sea. a–ClS (Rich), 1615.3 m, TOC=6.15%, Pyrite intercrystalline pore; b–ClMS (Rich), 1625.0 m, TOC=6.03%, Intergranular pore; c– ClS (Rich), 1634.1 m, TOC=6.17%, Dissolution pore, organic pore; d–SiS (Rich), 1640.2 m, TOC=7.96%, Organic pore; e–SiS (Rich), 1651.9 m, TOC=5.60%, Dissolution pore, intergranular pore, microcrack; f–ClMS (Rich), 1657.2 m, TOC=6.90%, Intercrystalline pore, intergranular pore; g–ClS (Rich), 1662.1 m, TOC=3.42%, Organic pore; h–ClMS (Medium), 1668.9 m, TOC=2.68%, Dissolution pore, organic pore, intercrystalline pore.

abundant organic pores after hydrocarbon generation, including a large number of micropores. Generally, mesopores contribute the most to the PV, followed by macropores (Figs. 6b, d). The contributions of meso- and macropores to the TPV of shales in Layer_1 are 64.31% and 34.97%, respectively, while those in Layer_2 are 74.22% and 23.06%, respectively. Thus, the mineral composition of shale has an important influence on pore type and development.

Petrographic analysis reveals that the Lower Permian is dominated by SiS, ClS, and ClMS shales. The TSSA of the ClS shales ranges from 0.34 m^2/g to 11.15 m^2/g (mean 3.51 m^2/g), and the TPV ranges from 2.52×10^{-3} cm^3/g to 12.89×10^{-3} cm^3/g (mean 7.29×10^{-3} cm^3/g). The TSSA of the ClMS shales ranges from 0.44 m^2/g to 7.63 m^2/g (mean 4.38 m^2/g), and the TPV ranges from 2.59×10^{-3} cm^3/g to 13.71×10^{-3} cm^3/g (mean 8.47×10^{-3} cm^3/g). The TSSA and TPV values of the ClMS shale samples are significantly higher than those of the ClS shales, indicating a better reservoir capacity of the ClMS shales in the study area.

N_2 adsorption saturation occurred when the relative pressure (p/p_0) tends to be close to 1, showing a typical type II nitrogen adsorption isotherms according to the IUPAC classification (Fig. 7). When $p/p_0 > 0.4$, a hysteresis loop appears between the adsorption and desorption branches. Type II adsorption isotherms are interpreted as the results of the monolayer and multilayer coverage at low (<0.4) and

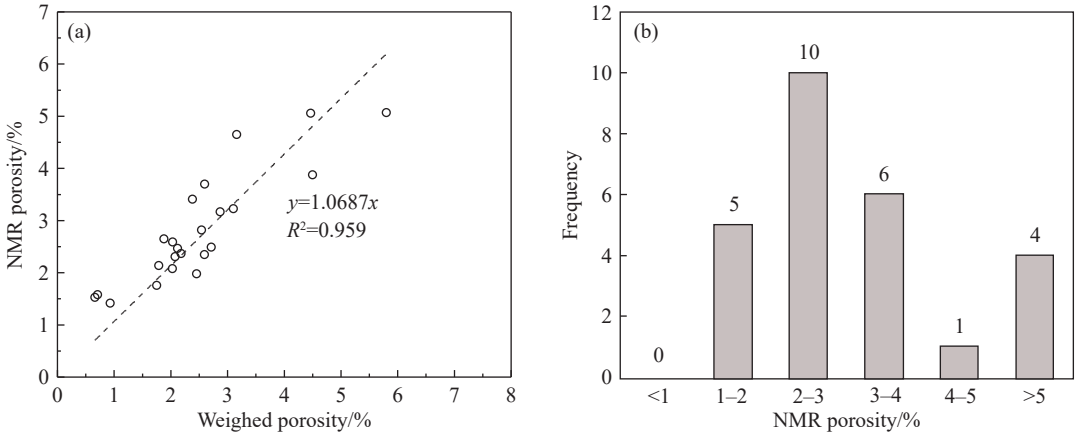

Fig. 5. a–Fitting relationship of nuclear magnetic resonance (NMR) porosity and weighed porosity, and b–statistical histogram of NMR porosity of the Lower Permian shales in the South Yellow Sea Basin.

Table 3. Statistical results of shale porosity and nitrogen adsorption experiments.

Layer	Depth/m	TOC	Weighted prorosity/%	NMR porosity/%	N_2 adsorption							Total SSA/(m^2/g)	Total PV/(10^{-3} cm^3/g)
					BET-SSA/(m^2/g)			PV/(10^{-3} cm^3/g)			d_{Na}/nm		
					Micro-	Meso-	Macro-	Micro-	Meso-	Macro-			
Layer_1	1600.5	3.23	2.18	2.37	0.0491	0.4623	0.0495	0.02	1.63	1.04	15.12	0.81	3.05
	1601.8	1.63	2.12	2.47	0.1761	2.6842	0.0948	0.08	5.77	1.87	10.18	3.19	8.11
	1603.4	1.5	2.87	3.17	0.1078	1.667	0.089	0.05	4.06	1.77	11.83	2.12	6.27
	1605.5	0.98	3.1	3.23	0.1539	2.3534	0.0966	0.07	5.71	2	10.89	2.98	8.12
	1609.7	1.53	/	5.04	0.1166	2.4908	0.0988	0.06	7.9	3.23	15.7	2.59	10.18
	1612.1	/	/	/	0.6998	3.8193	0.0946	0.33	7.28	1.91	5.62	8.11	11.39
	1612.4	1.41	5.8	5.07	0.0496	0.3465	0.0656	0.02	1.85	1.42	17.14	0.87	3.72
	1615.3	6.15	2.71	2.49	/	/	/	/	/	/	/	/	/
	1619.6	7.58	2.59	2.35	/	/	/	/	/	/	/	/	/
	1625	6.03	2.45	1.98	0	0.3712	0.0535	0	1.72	1.15	23.56	0.53	3.13
	1626.5	5.66	2.59	3.7	0	0.2442	0.0464	0	1.25	1	29.29	0.34	2.52
	1627.5	2.43	4.5	3.88	0.0106	1.0603	0.0878	0	3.85	1.88	16.06	1.53	6.16
	1630.2	5.1	1.79	2.14	0.0077	0.2558	0.0463	0	1.33	1.03	23.54	0.44	2.59
	1632.9	16.21	2.03	2.08	/	/	/	/	/	/	/	/	/
	1634.1	6.17	4.46	5.06	0	0.6199	0.0975	0	3.22	2.1	33.63	0.68	5.75
	1640.2	7.96	0.93	1.42	0.0227	0.1349	0.0237	0.01	0.69	0.54	18.44	0.3	1.38
	1645.3	6.41	0.66	1.53	/	/	/	/	/	/	/	/	/
Layer_2	1653.2	11.29	0.71	1.58	/	/	/	/	/	/	/	/	/
	1657.2	6.9	3.16	4.65	0.5542	2.8705	0.0815	0.27	6.96	2.63	5.97	7.55	11.27
	1661.5	3.63	2.38	3.41	0.1602	1.7954	0.0684	0.08	4.19	1.37	9.56	2.53	6.05
	1662.1	3.42	1.75	1.76	0.4654	3.0153	0.1015	0.22	6.45	2.05	6.63	6.18	10.24
	1664.8	1.61	2.08	2.31	0.3842	3.1312	0.0642	0.18	6.87	1.02	8.3	3.96	8.21
	1665.6	1.44	/	6.13	0.7518	4.8217	0.1489	0.36	9.7	2.92	7.91	6.93	13.71
	1666.3	6.84	1.88	2.65	1.1299	4.3651	0.1012	0.53	7.41	2.04	4.49	11.5	12.89
	1668.9	2.68	2.54	2.82	0.3016	1.7955	0.0549	0.14	3.7	1.15	6.43	3.91	6.29
	1670.7	4.33	2.03	2.59	0.691	3.8538	0.1145	0.42	7.49	2.36	6.28	7.63	11.98
	1678.6	1.43	/	3.03	0.0692	1.2448	0.0792	0.03	3.56	1.64	13.4	1.67	5.61

Notes: TOC: total organic carbon; NMR: nuclear magnetic resonance; BET: Brunauer-Emmett-Teller model; SSA: specific surface area; PV: pore volume.

medium (0.4–0.8) p/p_0, respectively, as well as capillary condensation at a high p/p_0 (>0.8), which suggests that meso-/macropores are developed in shales. Using the hysteresis loop classification of IUPAC, the Lower Permian shales are classified as H2 and H3 types, with H3 mainly occurring in Layer_1. The hysteresis loop characteristics indicate the development of a large number of mesopores in the shales, while the steep increase in the nitrogen adsorption capacity during the high-pressure phase may be closely related to the development of meso- and/or macropores. When p/p_0 reaches approximately 0.5, there is a clear turning point in the H2 type desorption branch, which may be related to the development of ink-bottle-shaped pores (Fig. 7). The H3 type is mainly characterized by almost parallel adsorption–desorption branches with narrow hysteresis loops, which mainly reflect slit-shaped and/or narrow pores (Fig. 7). The PSD of H2 shale is characterized by a bimodal distribution, with pore sizes ranging from 2 nm to 4 nm and 30 nm to 70 nm (Fig. 7). The

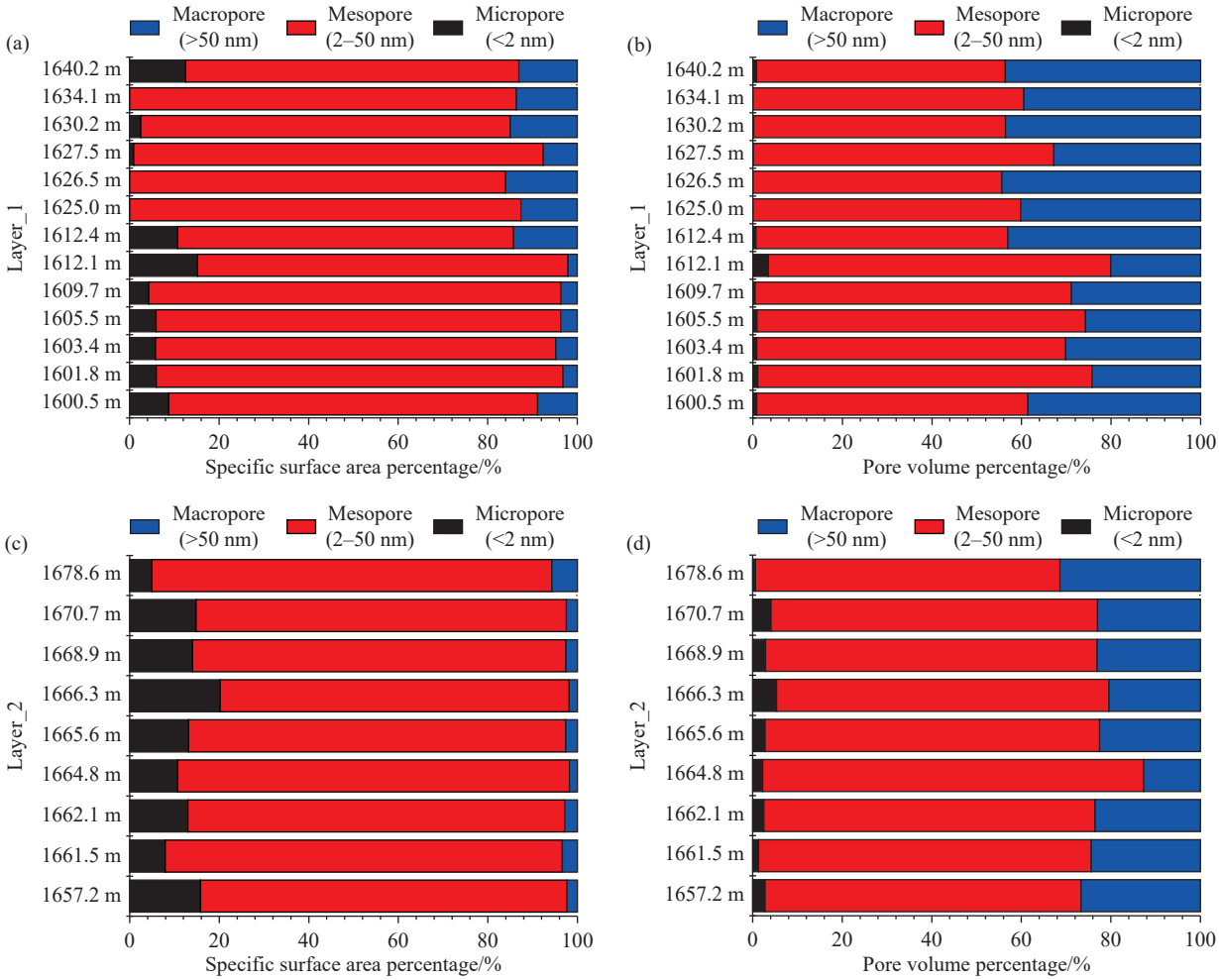

Fig. 6. Specific surface area and pore volume percentages with different pore sizes.

right peak of the PSD curve is significantly higher than the left peak, indicating that the mesopores of the H2 shale contribute more to the reservoir properties than the micropores do. The PSD curve of the H3 shale is characterized by a single peak, but the distribution range is large, with pore sizes ranging from 50 nm to 100 nm, reflecting the high percentage of macropores (Fig. 7).

4.2.4. Methane adsorption capacity of shales

A Langmuir-based excess sorption model was used to fit the excess sorption isotherm. The excess sorption isotherms fitted by the Langmuir-based excess sorption model for the shale samples are shown in Fig. 8a. The correlation coefficients exceed 0.99. V_{ex} increases rapidly with increasing pressure, reaching a maximum at approximately 8 MPa. The calculation of V_{ex} ignores the volume of adsorbed methane, and V_{ex} decreases with increasing pressure after reaching its maximum value (Fig. 8a). From Equ. (1), it can be deduced that V_{ex} will be approximately equal to zero when the density of the free methane approaches the density of the adsorbed methane under high-pressure conditions.

The fitted values of the density of adsorbed methane (ρ_{ads}) are in the range of 0.33–0.64 g/cm^3, with an average value of 0.41 g/cm^3 (Table 4). The absolute adsorption isotherms were well-fitted by the Langmuir sorption model, as shown in Fig. 8b. P_L ranges from 2.12 MPa to 3.55 MPa (mean 2.81 MPa) (Table 4), representing the pressure where the methane adsorbed amount equals half of the maximum methane sorption capacity (V_L). V_L ranges from 1.67 cm^3/g to 4.48 cm^3/g (mean 2.70 cm^3/g) (Table 4), indicating that the Lower Permian shales in the study area have good shale gas adsorption capacity. It should be noted that the methane sorption experiments in this study were performed on dry shale samples; therefore, the absolute methane sorption of the samples does not represent the methane sorption of the shale *in situ*.

4.2.5. Gas logging abnormalities of the Lower Permian shales in SYSB

The gas logging results showed significantly high anomalies in the Permian shales in the study area (Fig. 9). The gas logging results reveal that the Permian shales in the study area are generally gas-bearing. The average total gas in the 1580–1780 m interval is 7.4%, and the maximum value reached 66.2%. The main hydrocarbon gas in this section is methane, with an average content of 7.3% and a maximum value of 65.9% (Fig. 8). Methane accounts for approximately 98.6% of the total gas volume. It is a dry gas and is characterized by high maturity. The average contents of total gas and methane in the 1620–1680 m interval is 18.6% and

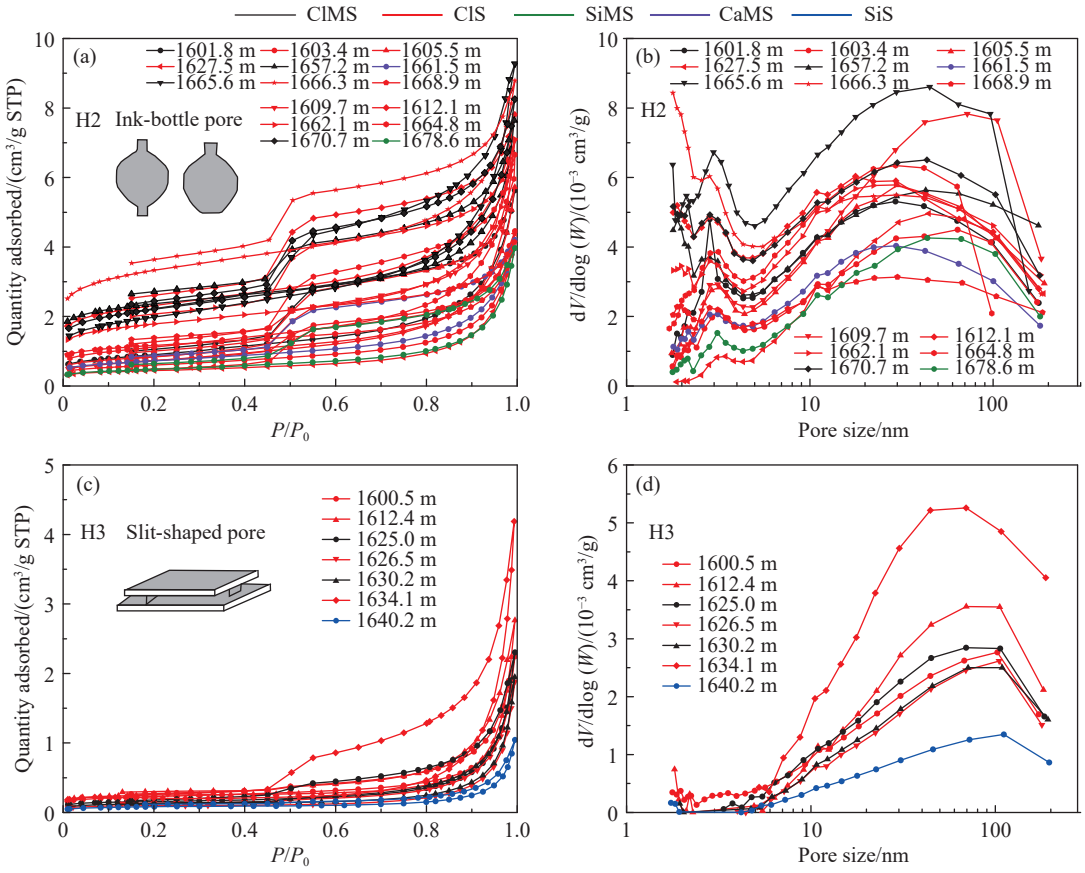

Fig. 7. a, c–Nitrogen adsorption–desorption isotherms, and b, d–shale pore size distribution.

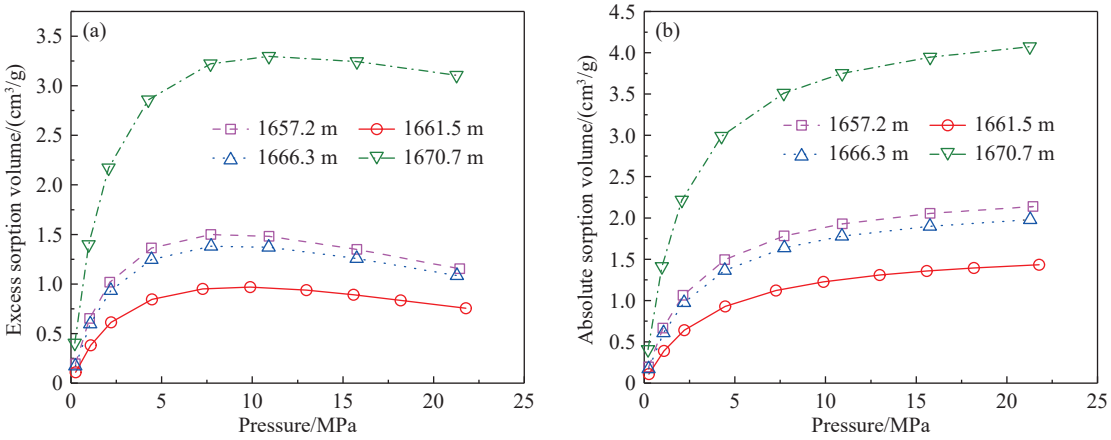

Fig. 8. a–Excess methane sorption isotherms, and b–absolute methane sorption isotherms of the Lower Permian shales in the South Yellow Sea Basin.

18.4%, respectively. In particular, the average contents of total gas and methane from 1640 m to 1658 m can reach up to 51.2% and 50.7%, respectively.

4.2.6. Fractal dimension results

Fractal dimensions D1 and D2 were calculated using the FHH model with the shale nitrogen adsorption data (Table 5). The nitrogen adsorption–desorption curves show a hysteresis loop at P/P_0 = 0.45, where two different adsorption mechanisms are exhibited. The fractal dimension D1, calculated when $P/P_0 < 0.45$, mainly reflects the roughness of the pore surface, while the fractal dimension D2, calculated when $P/P_0 > 0.45$, reflects the complexity of the pore structure.

The fitting coefficients of the fractal calculations are generally greater than 0.97, indicating good fractal characteristics. The fractal dimension D1 ranges from 2.5809 to 2.8095, with a mean value of 2.7019, and D2 ranges from 2.3505 to 2.8209, with a mean value of 2.6160. There are small variations in D1 throughout the Lower Permian shales, suggesting that the complexity of the pore surface does not significantly correlate with the petrography or mineral composition. However, the average D2 of Layer_2 is larger than that of Layer_1, which may be due to the more complex

pore structure caused by more dissolved pores, intergranular pores, and organic pores in Layer_2. Therefore, shale lithofacies have an important influence on the development of pore structures. The D1 of ClS shale ranges from 2.5809 to 2.8095 (mean: 2.7083), while D2 ranges from 2.3505 to 2.8209 (mean: 2.6238). The D1 of ClMS shale ranges from 2.6206 to 2.7930 (mean: 2.7133), while D2 is distributed from 2.4036 to 2.7675 (mean: 2.6226) (Table 5). D1 is larger than D2 for both the ClS and ClMS shales, probably because the micro- and mesopore types of the shale are mainly organic pores, resulting in a rougher pore surface.

Table 4. Fitting parameters of the Langmuir-based excess sorption model.

Depth/ m	Weight/ g	Langmuir volume/ (cm^3/g)	Langmuir pressure/ MPa	Density of adsorbed methane/ (g/cm^3)	Fitting coefficient/ R^2
1657.2	105.82	2.41	2.71	0.33	0.9979
1661.5	105.3	1.67	3.55	0.33	0.9965
1666.3	110.14	2.24	2.86	0.34	0.996
1670.7	104.48	4.48	2.12	0.64	0.9995

5. Discussion

5.1. Hydrocarbon generation potential of Lower Permian shale

The average TOC content of the Lower Permian shale is 5.99%. The average TOC of the section with the most

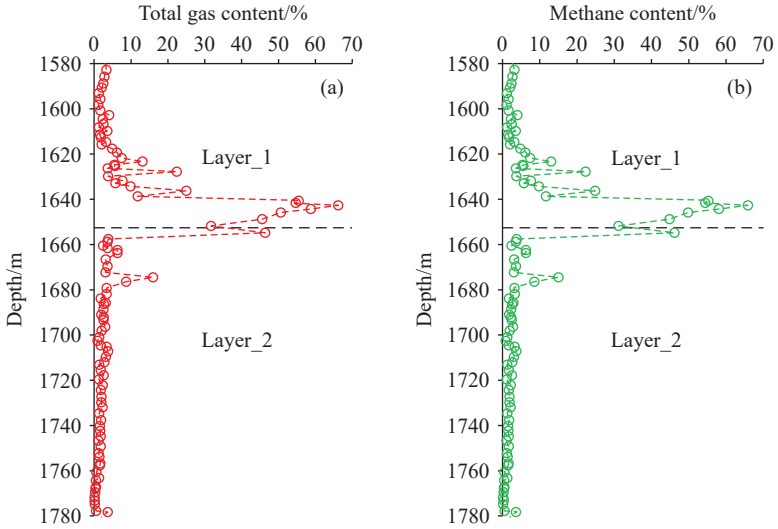

Fig. 9. Gas logging results of Lower Permian interval.

Table 5. Fractal dimension results calculated using the Frenkel-Halsey-Hill model.

Layer	Depth/m	P/P_0<0.45			P/P_0>0.45		
		Fractal fitting equation	R^2	D1	Fractal fitting equation	R^2	D2
Layer_1	1600.5	$y=-0.2880x-1.3419$	0.9944	2.712	$y=-0.4579x-1.4590$	0.9899	2.5421
	1601.8	$y=-0.3794x+0.0902$	0.996	2.6206	$y=-0.3356x+0.1674$	0.9765	2.6644
	1603.4	$y=-0.3461x-0.3345$	0.9969	2.6539	$y=-0.3772x-0.3159$	0.9854	2.6228
	1605.5	$y=-0.3464x+0.0065$	0.9979	2.6536	$y=-0.3645x+0.0356$	0.9815	2.6355
	1609.7	$y=-0.4191x-0.1054$	0.9973	2.5809	$y=-0.4252x-0.0706$	0.986	2.5748
	1612.1	$y=-0.2605x+0.9605$	0.9971	2.7395	$y=-0.2279x+0.9761$	0.9827	2.7721
	1612.4	$y=-0.1905x-1.3192$	0.8636	2.8095	$y=-0.5361x-1.6320$	0.9822	2.4639
	1625.0	$y=-0.2701x-1.7207$	0.9741	2.7299	$y=-0.5590x-1.8390$	0.9854	2.441
	1626.5	$y=-0.2461x-2.2315$	0.8402	2.7539	$y=-0.6492x-2.4691$	0.9851	2.3508
	1627.5	$y=-0.3039x-0.6655$	0.9935	2.6961	$y=-0.4690x-0.7235$	0.9836	2.531
	1630.2	$y=-0.2703x-1.9653$	0.9018	2.7297	$y=-0.5964x-2.2172$	0.987	2.4036
	1640.2	$y=-0.3665x-2.3470$	0.9154	2.6335	$y=-0.5404x-2.6237$	0.9891	2.4596
Layer_2	1657.2	$y=-0.2070x+0.9555$	0.9942	2.793	$y=-0.2325x+0.9023$	0.9963	2.7675
	1661.5	$y=-0.3294x-0.1609$	0.999	2.6706	$y=-0.3338x-0.1212$	0.9765	2.6662
	1662.1	$y=-0.2591x+0.6994$	0.9975	2.7409	$y=-0.2670x+0.6917$	0.9865	2.733
	1664.8	$y=-0.3690x+0.2956$	0.999	2.631	$y=-0.3135x+0.3856$	0.9653	2.6865
	1665.6	$y=-0.3239x+0.8394$	0.9999	2.6761	$y=-0.2925x+0.8683$	0.9786	2.7075
	1666.3	$y=-0.2337x+1.2918$	0.9905	2.7663	$y=-0.1791x+1.2900$	0.9888	2.8209
	1668.9	$y=-0.2377x+0.2656$	0.9978	2.7623	$y=-0.2474x+0.2496$	0.993	2.7526
	1670.7	$y=-0.2693x+0.9168$	0.9987	2.7307	$y=-0.2484x+0.9181$	0.9883	2.7516
	1678.6	$y=-0.3435x-0.5699$	0.9985	2.6565	$y=-0.4108x-0.5769$	0.9829	2.5892

significant gas logging anomaly (1640–1658 m) reaches 7.51%, indicating good hydrocarbon generation potential. This value is slightly higher than the average TOC of 6.48% (2.62%–11.47%) for the Barnett Shale and lower than the average TOC of 12.76% (9.99%–16.70%) for the Woodford Shale, America. In the Sichuan Basin of UYP, the main formations of shale gas development include the O_3w-S_1l, the Lower Cambrian Qiongzhusi Formation (ϵ_1q), and the Niutitang Formation (ϵ_1n). The TOC of the Lower Permian shales in the study area is close to that of O_3w-S_1l (2%–8.4%) but higher than that of the Lower Cambrian (Fig. 10). The current TOC threshold for commercial shale gas development is approximately 2%, and the Lower Permian shales in the study area meet the hydrocarbon generation conditions for the formation of large shale gas reservoirs.

Pg can also be used to evaluate the hydrocarbon generation potential of shales. The average Pg of the shales in the study area is 0.95 mg HC/g rock, which is close to that of the Longtan Formation shales in the Yangtze Platform but lower than that of the Barnett and Woodford shales (Fig. 10). This is because the Lower Permian in the study area is dominated by high- and over mature shales, and the hydrocarbon generation potential is largely depleted. Similarly, the Ro values of the source rocks in high-yielding shale gas fields in the Sichuan Basin, such as the Weiyuan, Huangjinba, Changning, and Fuling gas fields, generally exceed 2%, and the Pg values are also generally low. For example, the average Pg of shales in the ϵ_1q and ϵ_1n are 0.40 mg HC/g rock and 0.21 mg HC/g rock, respectively.

5.2. Evaluation of shale reservoir and its influencing factors

5.2.1. Reservoir capacity

Porosity is an important parameter for evaluating shale gas resources (Chalmers GR and Bustin RM, 2015; Kuang LC et al., 2022). The porosity of Lower Permian shales in the study area is generally greater than 2%, which is lower than that of the shales of Barnett, Marcellus, Haynesville, Eagle Ford, and Woodford in North America, but close to that of the shales of the S_1l and ϵ_1q in UYP and the Lower Permian shales of the onshore areas in LYP (Clarkson CR et al., 2013; Cao TT et al., 2018). The development of shale gas fields, including Fuling, Changning, Weiyuan, and Huangjinba in the UYP, has shown that their porosity satisfies the reservoir conditions for the formation of large shale gas fields. The TSSA (0.30–11.50 m^2/g, mean: 3.47 m^2/g) and TPV (1.38–13.71×10^{-3} cm^3/g, mean: 7.21×10^{-3} cm^3/g) of shales in the study area are lower than those of the marine shales in Weiyuan and Changning areas (Wang Y et al., 2016; Zhao WZ et al., 2016; Li A et al., 2017; Zhou SW et al., 2018). However, there are more meso- and macropores in the shales of the study area, which is favorable for the storage of free gas. It is concluded that the factors influencing the pore development of Paleozoic shales in the LYP mainly include: (1) The high-maturity shale produces a large number of organic pores after hydrocarbon generation; (2) the clay minerals have high relative content of illite with high pore volume and low content of chlorite with low pore volume; (3) the development of dissolution pores and microfractures in brittle minerals (siliceous minerals and calcareous minerals).

5.2.2. Influencing factors of pore structure

A strong positive correlation (R^2 = 0.8083) is observed between TSSA and TPV (Fig. 11). The SSA and TSSA of micro- and mesopores in the shale are also positively correlated, with correlation coefficients of 0.9587 and 0.8264, respectively. The PV and TPV of mesopores also show a strong positive correlation (R^2 = 0.9505), but the correlation between the PV and TPV of macropores is relatively low (R^2 = 0.6492). Overall, the contributions of micropores and

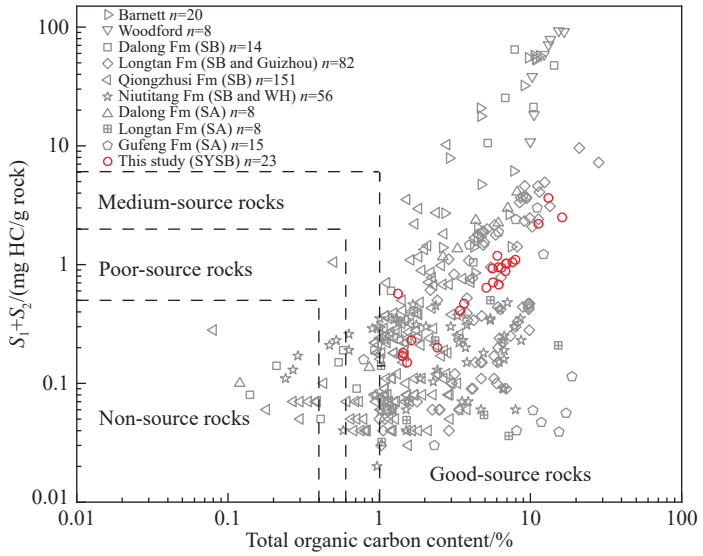

Fig. 10. Cross plot of total organic carbon and hydrocarbon generating potential of the Lower Permian shales in the South Yellow Sea compared to other shale formations. Other shale formations include Barnett and Woodford shales in America (Jarvie DM et al., 2007; Ko LT et al., 2018); Lower Cambrian Niutitang shales in Sichuan and northwest Hunan areas (Xi ZD et al., 2018; Xiao WY et al., 2021); Lower Cambrian Qiongzhusi shales in Sichuan (Li CR et al., 2021; Zhao L et al., 2022); Lower Permian Longtan shales in Sichuan and southwest Guizhou areas (He ZL et al., 2021; Zhang Q et al., 2020); Permian Dalong shales in Sichuan (Wei ZF et al., 2018); Permian Gufeng, Longtan and Dalong shales in South Anhui, China (Cao TT et al., 2018).

mesopores to the SSA are high, while the contribution of mesopores to the PV is high.

The development characteristics of organic matter and inorganic minerals have an important influence on shale pore structure (Gao ZY et al., 2021). There is no significant correlation between SSA and PV and TOC of meso-/macropores (Figs. 12a, b), but has a positive correlation for micropores, indicating that the high-mature organic matter mainly contributes to the development of micropores. Quartz is considered a rigid mineral that resists the compaction of shales, and SSA and PV should increase moderately as the quartz content increases. However, in this study, SSA and PV show a negative correlation with quartz content, particularly in the mesopores (Fig. 12), which may be related to the secondary enlargement and cementation of quartz. The illite and illite-smectite contents show a weak positive correlation with SSA and PV (Fig. 12), which may be due to the partial contribution of the micropores in these clay minerals. In addition, illite–smectite commonly fills dissolution pores, and its content may be an indicator of the development of dissolution pores, which increases SSA and PV.

5.2.3. Effect of shale pore structure on methane sorption capacity

Fig. 13 shows the relationships between the maximum absolute adsorption volume (V_L) and pore structure parameters. V_L is positively correlated with TSSA and TPV, indicating that shale with a larger surface area can adsorb more methane (Fig. 13). V_L is positively correlated with the SSA of macropores, while it is weakly correlated with the SSA of mesopores and micropores (Fig. 13). V_L is positively correlated with the PV of the micro-, meso-, and macropores (Fig. 13). Generally, micropore adsorption is mainly filling adsorption, whereas monolayer adsorption usually occurs in the meso-/macropores for the supercritical methane under experimental conditions. Therefore, the SSA, rather than PV, is the determining factor for methane adsorption in the meso-/macropores. In the study area, methane is mainly adsorbed in mesopores, followed by macropores; micropores do not significantly contribute to methane adsorption. This is consistent with the large number of organic and intergranular meso-/macropores observed in the SEM images (Fig. 4). In addition, V_L is positively correlated with the contents of organic matter and clay minerals (Fig. 13), which also indicates the importance of organic pores. The pore structure of the Lower Permian shales in the study area is relatively complex and is characterized by more organic pores and meso-/macropores. This phenomenon is more common in the over mature marine shales in South China. This implies that

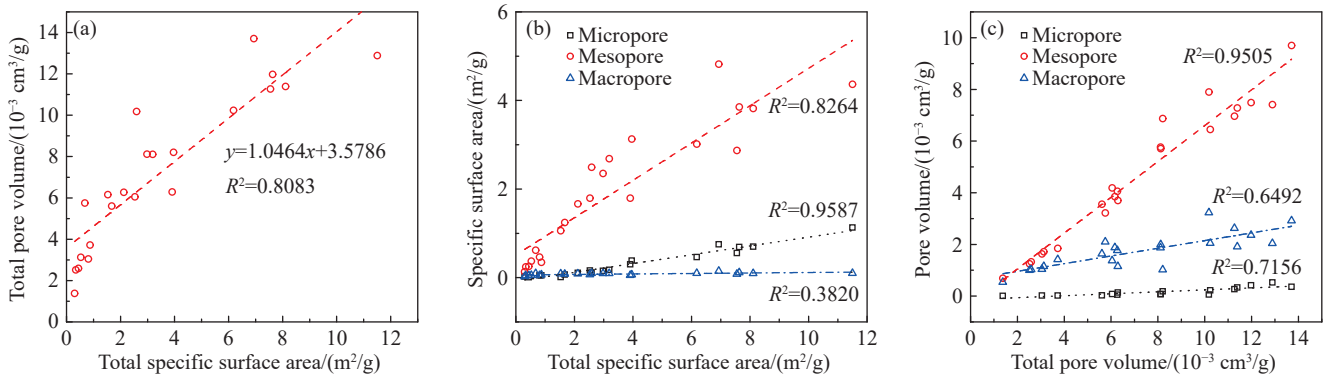

Fig. 11. a–Correlation between total specific surface area and total pore volume; b–correlation between specific surface area and total specific surface area; and c–correlation between pore volume and total pore volume of shales with different pore sizes.

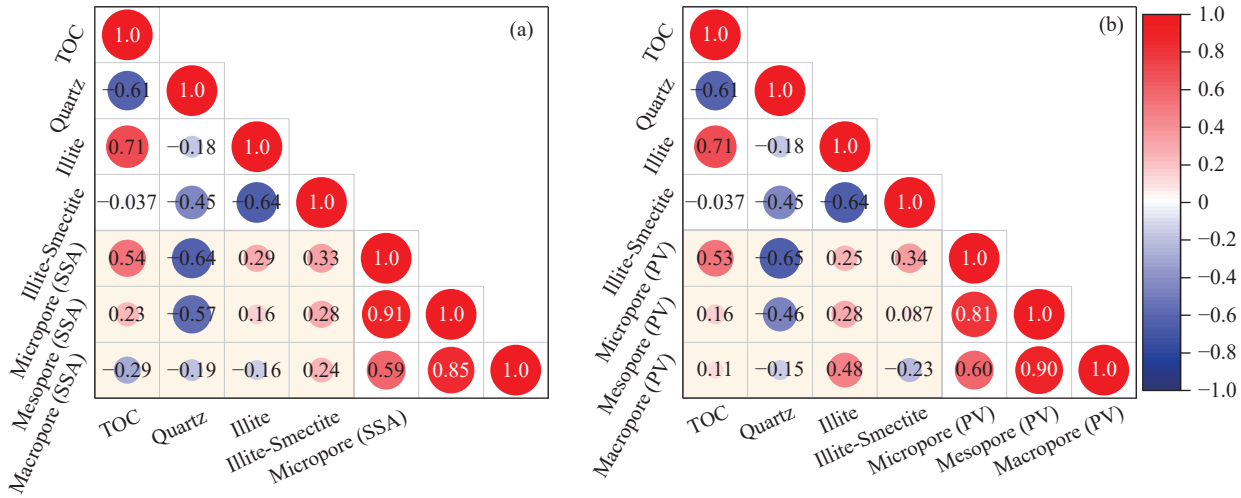

Fig. 12. Heat map shows the influence of shale organic matter and mineral composition on specific surface area (a) and pore volume (b) of shales.

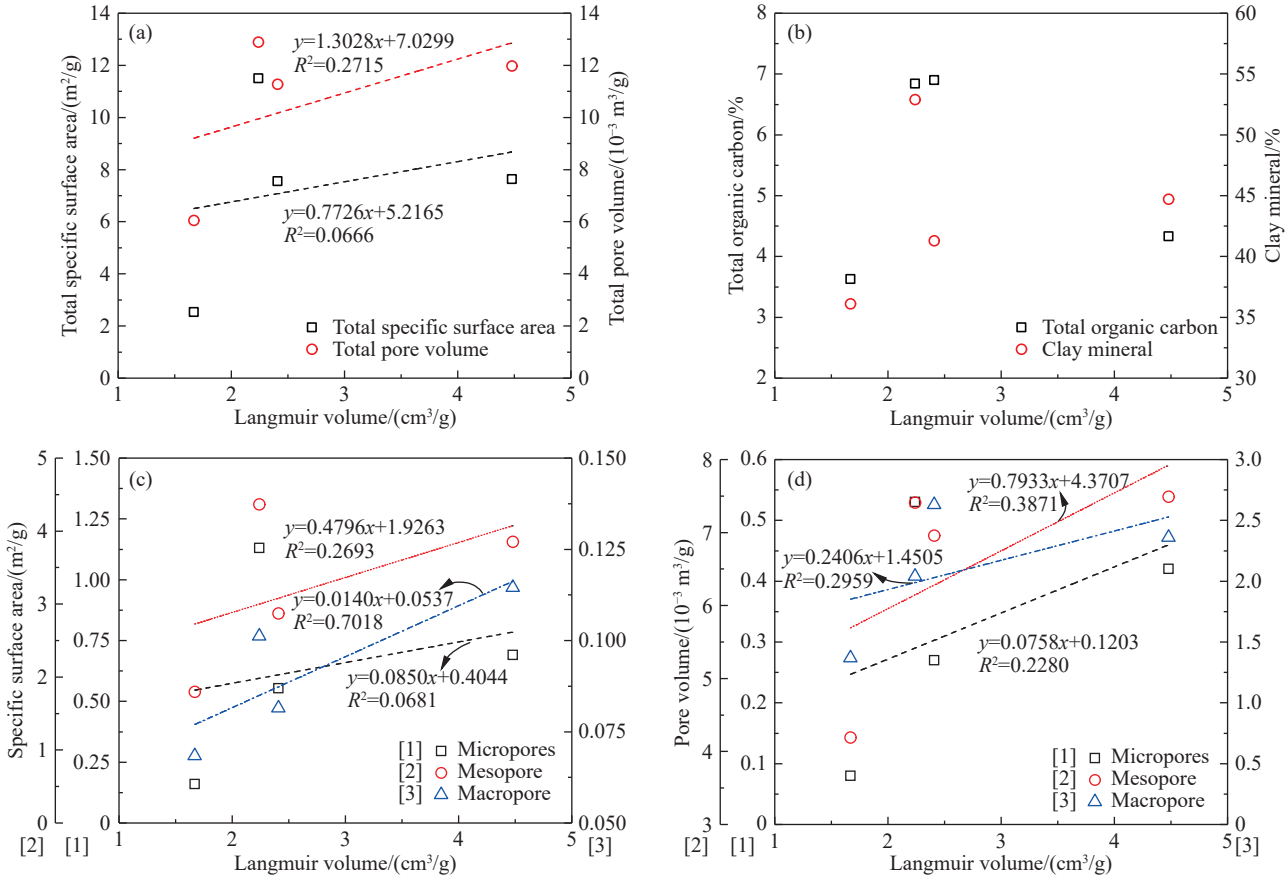

Fig. 13. Relationships between Langmuir volume and pore structure parameters (a, b) and the influences of total organic carbon and clay mineral on Langmuir volume (c, d).

the free gas may have made a major contribution to the total gas content in the study area.

5.2.4. Effect of shale mineral composition on shale gas development

Mineral composition has an important influence on the development of shale gas (Yasin Q et al., 2021; Li Y et al., 2022). The differences in mineral composition between the shales in the study area and typical shale gas fields are shown in Fig. 14. The average content of the shale clay minerals in the study area is 33.1%, with a high of content of illite having a high pore volume. This value is lower than those of the Ohio shale in the United States (average: 51.70%), Permian Longtan Formation shale in the Sichuan Basin (average: 47.93%), and LYP Wannan area (average: 60.23%). However, the clay mineral content in the study area is comparable to that in the Barnett, Woodford, and Bossier shales in the United States, the O_3w-S_1l, ϵ_1q and ϵ_1n shales in Sichuan Basin, and the Permian shales in Wannan area, South China (Fig. 14).

The content of brittle minerals (quartz, feldspar, pyrite, and carbonate minerals) in shales is an important indicator for determining the prospect of shale development (Zou CN et al., 2010; Yang W et al., 2021). The brittle mineral content in the shales of the study area is slightly higher than that of the Ohio Shale in the United States, the Permian Longtan Formation shales in the Sichuan Basin and Anhui Southern area, South China (Fig. 14), indicating favorable conditions for fracturing and development. In addition, Layer_2 is dominated by calcareous minerals, which not only facilitates the shale gas development but also improves the storage capacity. Overall, by comparing the mineral composition of typical shale gas fields, it is concluded that the shale in the study area is brittle and shallowly buried, meeting the geological conditions for low-cost development.

5.3. Potential evaluation of shale gas resource

In this study, a star diagram was used to evaluate the shale gas prospective potential (Jarvie DM et al., 2007; Du XB et al., 2015). TOC, porosity, thickness, brittle mineral content, *R*o, S_1+S_2, and TPV were selected and plotted in a star diagram. The results show that the Permian shale gas potential in the study area is comparable to that of the Barnett shale in the United States and Fuling shale in the Sichuan Basin, South China (Fig. 15). The shale gas potential of the Lower Permian shale in the study area is not as high as that of the Barnett shale but close to that of the Fuling shale gas field. The TOC, S_1+S_2, TPV, and thickness of the shales in the study area are higher than or close to the Fuling shale gas field, while the *R*o and Porosity indicators are slightly low. The relatively low *R*o is due to the fact that the CSDP-2 borehole is located in the uplifted area of the basin, which suffered significant uplift and denudation during the Indosinian period, resulting in a relatively shallow burial depth of the Lower Permian in the study area. However, in the northern and southern depressions

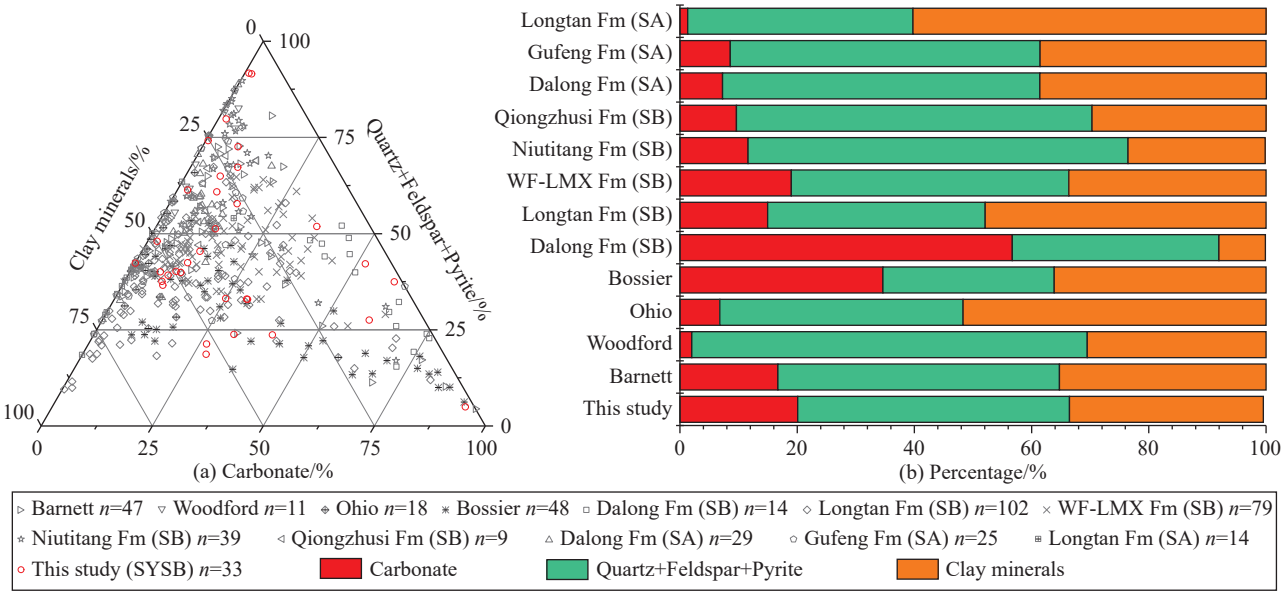

Fig. 14. Mineral composition (a) and percentage (b) of Lower Permian shales in the South Yellow Sea compared to other shale formations. Other shale formations are Barnett, Woodford, Ohio and Bossier shales in America (Ding WL et al., 2012; Jarvie DM et al., 2007; Ko LT et al., 2018); Dalong shales (Wei ZF et al., 2018), Longtan shales (Guo XS et al., 2019; He ZL et al., 2021), Wufeng-Longmaxi shales (Guan QZ et al., 2016; Hu HY et al., 2018; Li M et al., 2022; Wang QT et al., 2019), Niutitang shales (Xiao WY et al., 2021) and Qiongzhusi shales (Liu RY et al., 2022; Yang W et al., 2018) in Sichuan, China. Gufeng, Longtan and Dalong shales in south Anhui, China (Cao TT et al., 2018; Pan L et al., 2015; Xu LF et al., 2020).

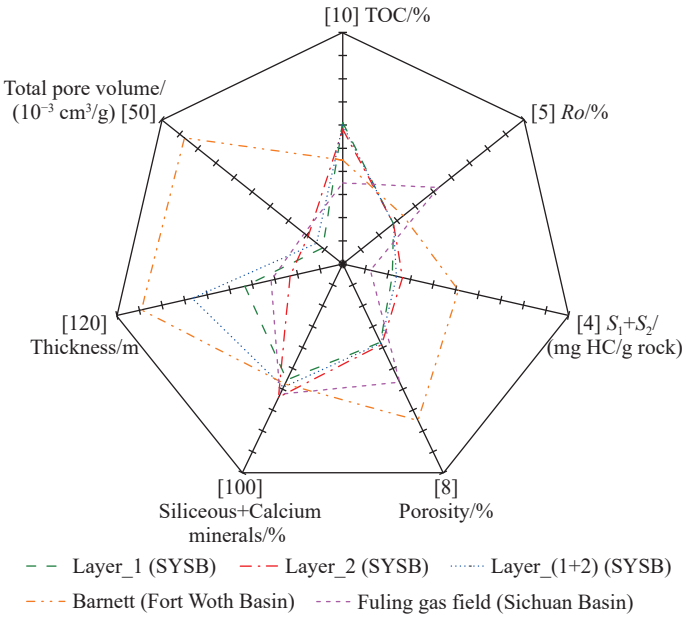

Fig. 15. Star diagram for assessing the shale gas potential in the Lower Permian of the South Yellow Sea compared to the Barnett shale in America (after Jarvie DM et al., 2007) and Fuling shale in Sichuan (after Guo XS et al., 2019).

of the South Yellow Sea, the Lower Permian is overlain by thick Mesozoic-Cenozoic rifted basin deposits, which are presumed to have higher *R*o and greater shale gas potential. In addition, the brittle mineral content (siliceous and calcareous minerals) of the shales in the study area is close to that of the Barnett and Fuling shales, indicating favorable shale gas development conditions. Although the shale gas potential of the study area is not as high as that of the Barnett shale, it is comparable to that of the Fuling shale gas field in the UYP. Thus, the shale gas potential of the Lower Permian in the study area is high.

6. Conclusions

(i) The upper part of the Lower Permian in SYSB is dominated by organic-rich siliceous shale, while the lower part is dominated by clay-mixed shale with a high content of calcareous minerals, and the clay minerals are rich in illite and mixed illite/smectite. The Lower Permian is dominated by type II_1−II_2 organic-rich shale, and the organic matter has entered the high-over mature evolution stage. A comparison of organic geochemical indicators with other typical shale gas fields shows that the Lower Permian shale in the study area

meet the conditions for generating abundant shale gas.

(ii) The pore types of the Lower Permian shales are dominated by organic pores, dissolution pores, and intergranular pores, followed by microfractures and intragrain pores of clay minerals, and the meso-/macropores are well developed. The analysis of average porosity, total specific surface area and pore volume of samples shows that the reservoir capacities of ClMS and ClS shales are relatively good. Shale lithofacies have an important influence on pore structure, and the fractal dimension D1 is larger than D2 for both ClS and ClMS shales, indicating that the roughness of the pore surface is significant. The shale pore structure is mainly controlled by the content of brittle minerals, as well as illite and mixed illite/smectite in the clay minerals. The methane gas adsorption isotherms are well fitted, and the average Langmuir volume obtained is 2.70 cm^3/g. Methane is mainly adsorbed in mesopores, followed by macropores.

(iii) The evaluation indicators of shale gas potential in the study area are generally close to those of the Fuling shale gas field in the Sichuan Basin. The Lower Permian shales are brittle and shallowly buried, meeting the geological conditions for low-cost development. In addition, this study speculates that the depression areas of the basin, which are overlain by thick Mesozoic-Cenozoic sediments, may have a higher maturity of organic matter and a greater exploration potential for shale gas.

CRediT authorship contribution statement

Yu-mao Pang, Zhao-meng Wei and Xing-wei Guo conceived of the presented idea. Zhao-meng Wei and Yu-mao Pang carried out the experiment. Yu-mao Pang and Zhao-meng Wei wrote the manuscript with support from Xing-wei Guo, Chuan-sheng Yang and Rui-shan Ma. Yu-mao Pang and Xun-hua Zhang helped supervise the project. All authors discussed the results and contributed to the final manuscript.

Declaration of competing interest

The authors declare no conflicts of interest.

Acknowledgments

This study is supported by the Natural Science Foundation of Shandong Province (ZR2023MD112) and financially supported by Laoshan Laboratory (LSKJ202203401).

References

Brunauer S, Emmett PH, Teller E. 1938. Adsorption of gases in multimolecular layers. Journal of the American Chemical Society, 60(2), 309–319. doi: 10.1021/ja01269a023.

Cai YD, Liu DM, Pan ZJ, Yao YB, Li JQ, Qiu YK. 2013. Pore structure and its impact on CH_4 adsorption capacity and flow capability of bituminous and subbituminous coals from NorthEast China. Fuel, 103, 258–268. doi: 10.1016/j.fuel.2012.06.055.

Cao TT, Deng M, Song ZG, Luo HY, Hursthouse AS. 2018. Characteristics and controlling factors of pore structure of the Permian shale in southern Anhui province, East China. Journal of Natural Gas Science and Engineering, 60, 228–245. doi: 10.1016/j.jngse.2018.10.018.

Cao TT, Song ZG, Wang SB, Xia J. 2016. Characterization of pore structure and fractal dimension of Paleozoic shales from the northeastern Sichuan Basin, China. Journal of Natural Gas Science and Engineering, 35, 882–895. doi: 10.1016/j.jngse.2016.09.022.

Chalmers GRL, Bustin RM. 2015. Porosity and pore size distribution of deeply-buried fine-grained rocks: Influence of diagenetic and metamorphic processes on shale reservoir quality and exploration. Journal of Unconventional Oil and Gas Resources, 12, 134–142. doi: 10.1016/j.juogr.2015.09.005.

Clarkson CR, Solano N, Bustin RM, Bustin AMM, Chalmers GRL, He L, Melnichenko YB, Radliński AP, Blach TP. 2013. Pore structure characterization of North American shale gas reservoirs using USANS/SANS, gas adsorption, and mercury intrusion. Fuel, 103, 606–616. doi: 10.1016/j.fuel.2012.06.119.

Ding WL, Li C, Li CY, Xu CC, Jiu K, Zeng WT. 2012. Dominant factor of fracture development in shale and its relationship to gas accumulation. Earth Science Frontiers, 19(2), 212–220 (in Chinese with English abstract).

Du XB, Song XD, Zhang MQ, Lu YC, Lu YB, Chen P, Liu ZH, Yang S. 2015. Shale gas potential of the Lower Permian Gufeng Formation in the western area of the Lower Yangtze Platform, China. Marine and Petroleum Geology, 67, 526–543. doi: 10.1016/j.marpetgeo.2015.05.031.

Gao ZY, Liang Z, Hu QH, Jiang ZX, Xuan QX. 2021. A new and integrated imaging and compositional method to investigate the contributions of organic matter and inorganic minerals to the pore spaces of lacustrine shale in China. Marine and Petroleum Geology, 127, 104962. doi: 10.1016/j.marpetgeo.2021.104962.

Gilder S, Courtillot V. 1997. Timing of the North-South China collision from new middle to late Mesozoic paleomagnetic data from the North China Block. Journal of Geophysical Research: Solid Earth, 102(B8), 17713–17727. doi: 10.1029/97jb01201.

Guan QZ, Dong DZ, Wang SF, Huang JL, Wang YM, Lu H, Zhang CC. 2016. Preliminary study on shale gas microreservoir characteristics of the Lower Silurian Longmaxi Formation in the southern Sichuan Basin, China. Journal of Natural Gas Science and Engineering, 31, 382–395. doi: 10.1016/j.jngse.2016.03.023.

Guo XS, Hu DF, Liu RB, Wei XF, Wei FB. 2019. Geological conditions and exploration potential of Permian marine–continent transitional facies shale gas in the Sichuan Basin. Natural Gas Industry B, 6(3), 198–204. doi: 10.1016/j.ngib.2018.10.002.

He ZL, Nie HK, Li SJ, Liu GX, Ding JH, Bian RK, Lu ZY. 2021. Differential occurence of shale gas in the Permian Longtan Formation of Upper Yangtze region constrained by plate tectonics in the Tethyan domain. Oil & Gas Geology, 42(1), 1–15 (in Chinese with English abstract). doi: 10.11743/ogg20210101.

He ZL, Nie HK, Zhang YY. 2016. The main factors of shale gas enrichment of Ordovician Wufeng Formation-Silurian Longmaxi Formation in the Sichuan Basin and its adjacent areas. Earth Science Frontiers, 23(2), 8–17 (in Chinese with English abstract). doi: 10.13745/j.esf.2016.02.002.

Hu H, Zhu YQ, Li SY, Li Z. 2021. Effects of green energy development on population growth and employment: Evidence from shale gas exploitation in Chongqing, China. Petroleum Science, 18(5), 1578–1588. doi: 10.1016/j.petsci.2021.08.013.

Hu HY, Hao F, Guo XS, Dai FY, Lu YC, Ma YQ. 2018. Investigation of methane sorption of overmature Wufeng-Longmaxi shale in the Jiaoshiba area, Eastern Sichuan Basin, China. Marine and Petroleum Geology, 91, 251–261. doi: 10.1016/j.marpetgeo.2018.01.008.

Jarvie DM, Hill RJ, Ruble TE, Pollastro RM. 2007. Unconventional shale-gas systems: The Mississippian Barnett shale of north-central Texas as one model for thermogenic shale-gas assessment. AAPG Bulletin, 91(4), 475–499. doi: 10.1306/12190606068.

Jiang ZX, Song Y, Tang XL, Li Z, Wang XM, Wang GZ, Xue ZX, Li X, Zhang K, Chang JQ, Qiu HY. 2020. Controlling factors of marine shale gas differential enrichment in Southern China. Petroleum Exploration and Development, 47(3), 661–673. doi: 10.1016/S1876-3804(20)60083-0.

Ko LT, Ruppel SC, Loucks RG, Hackley PC, Zhang TW, Shao DY. 2018. Pore-types and pore-network evolution in Upper Devonian-Lower Mississippian Woodford and Mississippian Barnett mudstones: Insights from laboratory thermal maturation and organic petrology. International Journal of Coal Geology, 190, 3–28. doi: 10.1016/j.coal.2017.10.001.

Kuang LC, Hou LH, Wu ST, Cui JW, Tian H, Zhang LJ, Zhao ZY, Luo X, Jiang XH. 2022. Organic matter occurrence and pore-forming mechanisms in lacustrine shales in China. Petroleum Science, 19(4), 1460–1472. doi: 10.1016/j.petsci.2022.03.005.

Levitz P, Van Damme H, Fripiat JJ. 1988. Growth of adsorbed multilayers on fractal surfaces. Langmuir, 4(3), 781–782. doi:

10.1021/la00081a052.
Li A, Ding WL, Zhou XH, Cao XY, Zhang M, Fu FQ, Chen E. 2017. Investigation of the methane adsorption characteristics of marine shale: A case study of lower Cambrian qiongzhusi shale in eastern Yunnan Province, South China. Energy & Fuels, 31(3), 2625–2635. doi: 10.1021/acs.energyfuels.6b03168.
Li CR, Pang XQ, Ma XH, Wang EZ, Hu T, Wu ZY. 2021. Hydrocarbon generation and expulsion characteristics of the Lower Cambrian Qiongzhusi shale in the Sichuan Basin, Central China: Implications for conventional and unconventional natural gas resource potential. Journal of Petroleum Science and Engineering, 204, 108610. doi: 10.1016/j.petrol.2021.108610.
Li M, Pang XQ, Xiong L, Hu T, Chen D, Zhao Z, Hui SS, Liu Y, Zhang SY. 2022. The main controlling factors on shale gas occurrence characteristics in deep and high-over mature shales: A case study of Silurian Longmaxi Formation in the Sichuan Basin, Southern China. Energy Reports, 8, 6901–6913. doi: 10.1016/j.egyr.2022.05.037.
Li Y, Chen JQ, Yang JH, Liu JS, Tong WS. 2022. Determination of shale macroscale modulus based on microscale measurement: A case study concerning multiscale mechanical characteristics. Petroleum Science, 19(3), 1262–1275. doi: 10.1016/j.petsci.2021.10.004.
Liu J, Zhang XH, Mei X, Zhao QH, Guo XW, Zhao WN, Liu JX, Saito Y, Wu ZQ, Li J, Zhu XQ, Chu HX. 2018. The sedimentary succession of the last ~3. 50 Myr in the western south Yellow Sea: Paleoenvironmental and tectonic implications. Marine Geology, 399, 47–65. doi: 10.1016/j.margeo.2017.11.005.
Li QQ, Xu S, Chen K, Song T, Meng FY, He S, Lu YC, Shi WZ, Gou QY, Wang YX. 2022. Analysis of shale gas accumulation conditions of the Upper Permian in the Lower Yangtze Region. Geology in China, 49(2), 383–397 (in Chinese with English abstract). doi: 10.12029/gc20220203.
Liu RY, Zhou W, Xu H, Zhou QM, Jiang K, Shang FH, Gao WL, Song WG, Liu DX, Zhao HS, Zhao X. 2022. Impact of minerals and sealing systems on the pore characteristics of the qiongzhusi formation shale in the southern Sichuan basin. ACS Omega, 7(18), 15821–15840. doi: 10.1021/acsomega.2c00869.
Nie HK, Li P, Dang W, Ding JH, Sun CX, Liu M, Wang J, Du W, Zhang PX, Li DH, Su HK. 2022. Enrichment characteristics and exploration directions of deep shale gas of Ordovician–Silurian in the Sichuan Basin and its surrounding areas, China. Petroleum Exploration and Development, 49(4), 744–757. doi: 10.1016/S1876-3804(22)60307-0.
Pan L, Xiao XM, Tian H, Zhou Q, Chen J, Li TF, Wei Q. 2015. A preliminary study on the characterization and controlling factors of porosity and pore structure of the Permian shales in Lower Yangtze region, Eastern China. International Journal of Coal Geology, 146, 68–78. doi: 10.1016/j.coal.2015.05.005.
Pang YM, Guo XW, Han ZZ, Zhang XH, Zhu XQ, Hou FH, Han C, Song ZG, Xiao GL. 2019. Mesozoic–Cenozoic denudation and thermal history in the Central Uplift of the South Yellow Sea basin and the implications for hydrocarbon systems: Constraints from the CSDP-2 borehole. Marine and Petroleum Geology, 99, 355–369. doi: 10.1016/j.marpetgeo.2018.10.027.
Pang YM, Shi BB, Guo XW, Zhang XH, Han ZZ, Cai LX, Xiao GL, Liu H. 2021. Source–reservoir relationships and hydrocarbon charging history in the central uplift of the south Yellow Sea basin (East Asia): Constrained by machine learning procedure and basin modeling. Marine and Petroleum Geology, 123, 104731. doi: 10.1016/j.marpetgeo.2020.104731.
Pfeifer P, Wu YJ, Cole MW, Krim J. 1989. Multilayer adsorption on a fractally rough surface. Physical Review Letters, 62(17), 1997–2000. doi: 10.1103/physrevlett.62.1997.
Tatlıer M, Erdem-Şenatalar A. 1999. Method to evaluate the fractal dimensions of solid adsorbents. The Journal of Physical Chemistry B, 103(21), 4360–4365. doi: 10.1021/jp983179x.
Wang JY, Guo SB. 2021. Study on the relationship between hydrocarbon generation and pore evolution in continental shale from the Ordos Basin, China. Petroleum Science, 18(5), 1305–1322. doi: 10.1016/j.petsci.2021.01.002.
Wang QT, Wang TL, Liu WP, Zhang J, Feng Q, Lu H, Peng PA. 2019. Relationships among composition, porosity and permeability of Longmaxi Shale reservoir in the Weiyuan Block, Sichuan Basin, China. Marine and Petroleum Geology, 102, 33–47. doi: 10.1016/j.marpetgeo.2018.12.026.
Wang Y, Zhu YM, Liu SM, Zhang R. 2016. Pore characterization and its impact on methane adsorption capacity for organic-rich marine shales. Fuel, 181, 227–237. doi: 10.1016/j.fuel.2016.04.082.
Wei ZF, Wang YL, Wang G, Sun ZP, Xu L. 2018. Pore characterization of organic-rich Late Permian Da-long Formation shale in the Sichuan Basin, southwestern China. Fuel, 211, 507–516. doi: 10.1016/j.fuel.2017.09.068.
Xi ZD, Tang SH, Wang J. 2018. The reservoir characterization and shale gas potential of the Niutitang formation: Case study of the SY well in northwest Hunan Province, South China. Journal of Petroleum Science and Engineering, 171, 687–703. doi: 10.1016/j.petrol.2018.08.002.
Xiao WY, Cao J, Liao ZW, Hu G, Zuo ZX, Hu K. 2021. Elemental geochemistry proxies recover original hydrogen index values and total organic carbon contents of over-mature shales: Lower Cambrian South China. Chemical Geology, 562, 120049. doi: 10.1016/j.chemgeo.2020.120049.
Xu LF, Zhang JC, Ding JH, Liu T, Shi G, Li XQ, Dang W, Cheng YS, Guo RB. 2020. Pore structure and fractal characteristics of different shale lithofacies in the dalong formation in the western area of the Lower Yangtze platform. Minerals, 10(1), 72. doi: 10.3390/min10010072.
Yang W, Xu L, Chen DX, Jiang ZX, Zhang ZY, Hao B, Zuo RS, Wang QY, Chen R. 2021. How argillaceous reservoirs exhibit better quality than silty mudstones? Anomalous behavior of shale gas-bearing properties of continental fine-grained sediments in Southwest China and its possible forcing mechanisms. Petroleum Science, 18(6), 1589–1610. doi: 10.1016/j.petsci.2021.09.032.
Yang W, Zuo RS, Jiang ZX, Chen DX, Song Y, Luo Q, Wang QY, Zhu HJ. 2018. Effect of lithofacies on pore structure and new insights into pore-preserving mechanisms of the over-mature Qiongzhusi marine shales in Lower Cambrian of the southern Sichuan Basin, China. Marine and Petroleum Geology, 98, 746–762. doi: 10.1016/j.marpetgeo.2018.09.020.
Yasin Q, Sohail GM, Liu KY, Du QZ, Boateng CD. 2021. Study on brittleness templates for shale gas reservoirs-a case study of Longmaxi shale in Sichuan Basin, Southern China. Petroleum Science, 18(5), 1370–1389. doi: 10.1016/j.petsci.2021.09.030.
Zhang JZ, Li XQ, Zhang XQ, Zhang M, Cong GS, Zhang GW, Wang FY. 2018. Geochemical and geological characterization of marine–continental transitional shales from Longtan Formation in Yangtze area, South China. Marine and Petroleum Geology, 96, 1–15. doi: 10.1016/j.marpetgeo.2018.05.020.
Zhang Q, Grohmann S, Xu XC, Littke R. 2020. Depositional environment and thermal maturity of the coal-bearing Longtan Shale in southwest Guizhou, China: Implications for shale gas resource potential. International Journal of Coal Geology, 231, 103607. doi: 10.1016/j.coal.2020.103607.
Zhao L, Liu SG, Li GQ, Zhang ML, Liang X, Li JX, Xu JL. 2022. Sedimentary environment and enrichment of organic matter during the deposition of qiongzhusi formation in the upslope areas—a case study of W207 well in the Weiyuan area, Sichuan basin, China. Frontiers in Earth Science, 10, 867616. doi: 10.3389/feart.2022.867616.
Zhao WZ, Li JZ, Yang T, Wang SF, Huang JL. 2016. Geological difference and its significance of marine shale gases in South China. Petroleum Exploration and Development, 43(4), 547–559. doi: 10.1016/S1876-3804(16)30065-9.
Zheng HJ, Zhou DR, Yin QC, Xiong QQ, Wang ZP, Fang CG, Teng L, Shao W, Wang YJ. 2020. New progress and breakthrough difficulties on shale gas geological survey in the Lower Yangtze area. Journal of Geomechanics, 26(6), 852–871 (in Chinese with English abstract). doi: 10.12090/j.issn.1006-6616.2020.26.06.067.
Zhou SW, Xue HQ, Ning Y, Guo W, Zhang Q. 2018. Experimental study of supercritical methane adsorption in Longmaxi shale: Insights into the density of adsorbed methane. Fuel, 211, 140–148. doi: 10.1016/j.fuel.2017.09.065.
Zou CN, Dong DZ, Wang SJ, Li JZ, Li XJ, Wang YM, Li DH, Cheng KM. 2010. Geological characteristics and resource potential of shale gas in China. Petroleum Exploration and Development, 37(6), 641–653. doi: 10.1016/S1876-3804(11)60001-3.
Zou CN, Dong DZ, Wang YM, Li XJ, Huang JL, Wang SF, Guan QZ, Zhang CC, Wang HY, Liu HL, Bai WH, Liang F, Lin W, Zhao Q, Liu DX, Yang Z, Liang PP, Sun SS, Qiu Z. 2016. Shale gas in China: Characteristics, challenges and prospects (II). Petroleum Exploration and Development, 43(2), 182–196. doi: 10.1016/S1876-3804(16)30022-2.
Zou CN, Zhao Q, Cong LZ, Wang HY, Shi ZS, Wu J, Pan SQ. 2021. Development progress, potential and prospect of shale gas in China. Natural Gas Industry, 41(1), 1–14 (in Chinese with English abstract). doi: 10.3787/j.issn.1000-0976.2021.01.001.